The Astrophysical Journal, 1012:15 (26pp), 2026 November 20 https://doi.org/10.3847/1538-4357/aea6d7
© 2026. The Author(s). Published by the American Astronomical Society.
OPEN ACCESS

The Deep Newtonian Regime in Late-time Blast Waves: Inevitable Transition and Distinct Flux Signatures

Sk. Minhajur Rahaman[1], Jonathan Granot[1,2,3], and Paz Beniamini[4,1,3]
[1] Astrophysics Research Center of the Open University (ARCO), The Open University of Israel, P.O Box 808, Ra'anana 4353701, Israel
[2] Astroparticule et Cosmologie (APC), CNRS – Université Paris Cité, F-75013 Paris, France
[3] Department of Physics, The George Washington University, 725 21st Street NW, WA, DC 20052, USA
[4] Department of Natural Sciences, The Open University of Israel, P.O Box 808, Ra'anana 4353701, Israel
Received 2026 April 26; revised 2026 August 22; accepted 2026 September 11; published 2026 November 10

Abstract

In many astrophysical transients, outflows drive shocks into the ambient medium, accelerating electrons to nonthermal energy distributions that produce broadband synchrotron emission. At late times, even initially collimated relativistic jets evolve into quasi-spherical Newtonian blast waves. As the shock decelerates, the post-shock internal energy per particle decreases; below a critical velocity $\beta_{\rm DN} \approx 0.2$, only a fraction $\xi_e < 1$ of electrons are accelerated to relativistic energies, defining the deep Newtonian (DN) regime. We develop a unified analytic framework for synchrotron emission in this phase, applicable to both single-velocity and stratified ejecta. For gamma-ray burst afterglows in a uniform medium, the DN transition occurs at $t_{\rm DN} \approx 3.7\, E_{51}^{1/3} n_0^{-1/3}$ yr, yielding a shallower decay by $\delta\alpha = 6(p-2)/5$ relative to standard Newtonian predictions. For kilonova remnants ($E_0 = 10^{50.5}$ erg, $M_{\rm ej} = 0.1\, M_\odot$), the DN phase begins prior to deceleration; neglecting it underestimates radio flux by factors of ∼3–5 during coasting and even more thereafter. Magnetar-boosted remnants ($E \sim 10^{52}$ erg) should reach $\sim 10-100\,\mu$Jy at 3 GHz at ∼40Mpc, though limits on GW170817 already disfavor a long-lived millisecond magnetar. In core-collapse supernovae in a wind medium ($\rho \propto r^{-k}$), the peak luminosity remains constant during coasting, while $\nu_{\rm pk} \propto t^{-1}$; for SN 2023ixf, we find $k = 1.29 \pm 0.14$. The DN spectral energy distribution typically satisfies $\nu_m < \nu_{\rm sa} < \nu_c$, peaking at sub-GHz frequencies where LOFAR and SKA-low are most sensitive. Even nondetections place robust constraints on ambient density and outflow energetics.

Unified Astronomy Thesaurus concepts: High energy astrophysics (739); Non-thermal radiation sources (1119); Transient sources (1851); Compact objects (288); Gamma-ray bursts (629); Core-collapse supernovae (304)

1. Introduction

Outflows in astrophysical transients including gamma-ray bursts (GRBs), kilonova remnants (KNRs), magnetar giant flares (MGFs), core-collapse supernovae (CCSNe), and superluminous supernovae (SLSNe) drive forward shocks into the ambient medium, accelerating nonthermal electrons and producing broadband synchrotron (afterglow) emission. A ubiquitous late-time feature in these outflows is that the shock eventually decelerates, becomes Newtonian and approaches spherical symmetry, even if it was initially launched as a highly collimated relativistic jet. In the Newtonian spherical phase, the post-shock internal energy per electron decreases, and when the outflow speed drops below a critical value ($\beta_{\rm DN}$; see Equation (8)), there is enough internal energy to accelerate only a small fraction ($\xi_e < 1$) of the electrons to relativistic energies. This defines the onset of the *deep Newtonian* (DN) regime. A self-consistent physical treatment must take into account the modifications in the particle energy distribution and the subsequent emission properties in this phase. Although the DN phase has been noted in several works on GRB (Y. F. Huang & K. S. Cheng 2003; L. Sironi & D. Giannios 2013; P. Beniamini et al. 2022), MGF (J. Granot et al. 2006), KNR (A. Kathirgamaraju et al. 2019; S. K. Acharya et al. 2025), CCSNe (R. Barniol Duran et al. 2016), in a vast majority of the relevant scientific literature, the DN phase is overlooked, despite its potential to modify both the flux normalization and the late-time rise and decay (see Section 4).

Currently, a generalized treatment of the DN regime is lacking. Existing studies are object-specific, and for simplicity, they typically assume a single ejecta velocity and a uniform ambient density, whereas theoretical models and simulations indicate stratified ejecta and nonuniform ambient media. The broadband DN spectral evolution is poorly explored. The DN phase during the coasting stage also remains poorly explored, and the self-absorption frequency, $\nu_{\rm sa}$, is generally only approximately estimated. As we demonstrate here, the low-frequency spectral turnover and peak spectral luminosity occur at $\nu_{\rm sa}$, making its accurate determination essential for late-time observational strategies.

In this work, we present a unified framework for the DN regime, applicable to both single-velocity and stratified ejecta interacting with a variety of ambient density profiles. We compute the synchrotron spectrum across all relevant dynamical phases, providing a tool to assess detectability and diagnostic potential. The paper is organized as follows: In Section 2, we describe DN shock dynamics and the resulting spectra and light curves. In Section 3, we explore the parameter space for transients expected to enter the DN phase. Finally, in Section 4, we summarize our main results and discuss observational strategies.

2. DN Regime

In this section, we motivate the DN phase from shock hydrodynamics and explore the temporal effects on the light curves and the spectrum.

Original content from this work may be used under the terms of the Creative Commons Attribution 4.0 licence. Any further distribution of this work must maintain attribution to the author(s) and the title of the work, journal citation and DOI.

We first provide a brief summary of the DN phase and the motivation for the prescription adopted in this work. The DN phase was first introduced phenomenologically by Y. F. Huang & K. S. Cheng (2003) in studies of late-time GRB afterglows, where it was recognized that the commonly adopted electron distribution, $dN/d\gamma_e \propto \gamma_e^{-p}$, is appropriate for relativistic electrons with $\gamma_e \gg 1$, but becomes inadequate as γ_e approaches unity. They therefore introduced the phenomenological prescription $dN/d\gamma_e \propto (\gamma_e - 1)^{-p}$, corresponding to a power-law electron kinetic energy distribution. In the nonrelativistic limit, $\gamma_e - 1 \simeq \beta_e^2/2$, such that this becomes a power law in β_e^2. Consequently, in this prescription, both the particle number and energy content are dominated by the minimum electron velocity, $\beta_{e,min} \propto \beta_{sh}$, such that the accelerated-particle number fraction ξ_e and energy fraction ϵ_e both decrease as the shock velocity β_{sh} decreases. This behavior is illustrated in the right panels of Figures A1 and A2, and is further quantified in Figure A2 in Appendix A. Thus, in the DN regime, both the number of relativistic particles and the energy carried by them decline substantially as the shock decelerates. As discussed below, however, for the prescription adopted in this work, ϵ_e can be treated as constant in the DN phase.

A physically motivated alternative was subsequently proposed by J. Granot et al. (2006) in their study of the radio afterglow of the 27 December 2004 giant flare from the magnetar SGR 1806−20 (see Section 3.1 for details). They showed that the observed radio emission could be reproduced by assuming that a constant fraction ϵ_e of the injected energy is transferred to accelerated particles characterized by an effective energy $\gamma_m - 1 \sim 1$, while the fraction of accelerated particles, ξ_e, decreases as the shock becomes increasingly nonrelativistic. This prescription is equivalent to a power-law distribution in the accelerated particles' dimensionless momentum, $dN/du_e \propto u_e^{-p}$ for $u_e \geqslant u_{e,min}$ where $u_e \equiv \gamma_e\beta_e$. In this case, for $u_{e,min} \ll 1$, the particle number density of particles is dominated by $u_e \sim u_{e,min}$, while the energy density is dominated by $u_e \sim 1$ or $\gamma_{dn} \sim 2 - 3$ (see left panel of Figure A1 and Figure A2 in Appendix A). Such a momentum-space power law is also naturally motivated by the theory of diffusive shock acceleration (e.g., A. R. Bell 1978; R. D. Blandford & J. P. Ostriker 1978; R. Blandford & D. Eichler 1987). In this formulation, the transition to the DN regime is not imposed through an ad hoc modification of the electron energy distribution at subrelativistic values of γ_e; instead, the power-law distribution is maintained in momentum space as the characteristic particle energy becomes nonrelativistic. L. Sironi & D. Giannios (2013) subsequently adopted the same prescription and showed that late-time radio afterglows of GRBs, which are expected to enter the DN phase, are more naturally described by a power-law distribution in momentum rather than in Lorentz factor.

Particle-in-cell (PIC) and hybrid kinetic simulations have been instrumental in uncovering the microphysics of mildly relativistic to nonrelativistic collisionless shocks (A. Spitkovsky 2008; D. Caprioli & A. Spitkovsky 2014; A. Bykov et al. 2022). These simulations have demonstrated that such shocks produce complex particle distributions consisting of a thermal Maxwellian core, a suprathermal population, and a developing nonthermal power-law tail. However, the primary strength of current kinetic simulations lies in describing the *initial stages of particle injection and acceleration*, rather than obtaining fully converged asymptotic particle distributions relevant for late-time astrophysical emission.

The formation of a steady-state nonthermal population is intrinsically a long-timescale process. While kinetic simulations successfully capture shock formation, particle reflection, and suprathermal particle generation, the development of the high-energy tail requires repeated shock crossings and sustained nonlinear interaction with self-generated turbulence over many acceleration cycles. Both the particle momentum distribution and the magnetic fields in the shock upstream and downstream have not yet reached a steady state in these simulations, and they keep evolving together. Current kinetic simulations typically follow the evolution of the shock for a limited number of ion gyroperiods, $t \sim 10^2 - 10^4\Omega_{ci}^{-1}$, depending on the numerical method, the dimensionality, and the shock parameters. Over such timescales, the maximum particle energy, normalization of the nonthermal tail, and fraction of particles participating in acceleration can continue to evolve beyond the accessible simulation duration.

Moreover, computational limitations often require reduced ion-to-electron mass ratios $m_p/m_e \ll 1836$, which decrease the separation between electron and ion kinetic scales and can modify electron heating and injection physics (A. Ligorini et al. 2021a, 2021b; M. Rassel et al. 2023). Furthermore, many kinetic investigations are performed in one or two spatial dimensions (see S. Gupta et al. 2024 for a detailed discussion), where the restricted magnetic-field geometry can suppress the full three-dimensional turbulent cascade and alter particle scattering. Consequently, the acceleration efficiency and spectral properties obtained in reduced-dimensionality simulations may not fully represent the asymptotic behavior of real astrophysical shocks. Given these limitations, in this work we adopt the prescription developed by J. Granot et al. (2006) and L. Sironi & D. Giannios (2013). If future PIC or hybrid kinetic simulations demonstrate a different asymptotic behavior in the DN regime, the prescription adopted here can be revised accordingly.

For the remainder of this analysis, all primed quantities are defined in the comoving frame. The LF of nonthermal electrons, denoted by γ_e, is left unprimed to align with standard notation in the literature, despite representing a comoving quantity. For the rest of the work, we adopt the usual convention $Q_x = Q/10^x$ in cgs units.

2.1. Microphysical Parameters

We assume the distribution of shock-accelerated nonthermal electrons in the comoving frame follows a power law of the form

$$\frac{dn'}{d\gamma_e} \propto \gamma_e^{-p} \qquad \text{for} \qquad \gamma_m < \gamma_e < \gamma_M, \tag{1}$$

where n' is the number density and p is the *power-law index*, bounded between a minimum LF γ_m and a maximum LF γ_M. These nonthermal electrons constitute a fraction ξ_e of the total number of electrons and carry a fraction ϵ_e of the comoving internal energy density e'_{int}.

The average LF of this distribution is given by

$$\langle\gamma_e\rangle \equiv \frac{\int_{\gamma_m}^{\gamma_M} \gamma_e \frac{dn'}{d\gamma_e} d\gamma_e}{\int_{\gamma_m}^{\gamma_M} \frac{dn'}{d\gamma_e} d\gamma_e} = \frac{\gamma_m}{G(p)}, \tag{2}$$

where the dimensionless function $G(p)$ captures the ratio $\gamma_m/\langle\gamma_e\rangle$ and is defined as

$$G(p) \equiv \frac{\gamma_m}{\langle\gamma_e\rangle} = \frac{(p-2)}{(p-1)}\left[\frac{1-(\gamma_M/\gamma_m)^{1-p}}{1-(\gamma_M/\gamma_m)^{2-p}}\right] \approx \frac{p-2}{p-1}, \quad \text{for} p > 2 \text{and} \gamma_M \to \infty. \quad (3)$$

The LF γ_m is determined by requiring that the kinetic energy of the nonthermal electrons equals $\epsilon_e e'_{int}$. This yields

$$\frac{\gamma_m}{G(p)} - 1 = \epsilon_e \xi_e^{-1}\left(\frac{m_p}{m_e}\right)(\Gamma_{ud} - 1), \quad (4)$$

where Γ_{ud} is the relative LF between the upstream and downstream fluids. A straightforward way to see this is to note that a fraction ϵ_e of the mean internal energy per proton, $(\Gamma_{ud}-1)m_p c^2$, is transferred to ξ_e power-law electrons with a mean internal energy $(\langle\gamma_e\rangle - 1)m_e c^2$. Assuming $\gamma_m \gg 1$, the expression simplifies to

$$\gamma_m \approx 1836\, G(p)\, \epsilon_e\, \xi_{e0}^{-1}(\Gamma_{ud} - 1). \quad (5)$$

As the shock propagates into the ambient medium, the available internal energy per baryon $\Gamma_{ud} - 1$ gradually decreases (in the Newtonian limit, $\Gamma_{ud} - 1 \approx \frac{1}{2}\beta_{ud}^2 \ll 1$, where β_{ud} is the relative upstream to downstream normalized velocity). This gives

$$\gamma_m \approx 918\, G(p)\, \epsilon_e\, \xi_{e0}^{-1}\beta_{ud}^2. \quad (6)$$

For an initially constant $\xi_e = \xi_{e0}$, Equation (6) shows that this would eventually lead to $\gamma_m - 1 < 1$, suggesting that an increasing fraction of particles becomes nonrelativistic. Indeed, the DN regime is established when $\gamma_m = \gamma_{dn} = \sqrt{2}$, a fixed fiducial value corresponding to mildly relativistic electrons (which corresponds to $u_e = \gamma_e\beta_e = 1$). For the rest of the analysis, we assume a fixed value of $\gamma_{dn} = \sqrt{2}$. Beyond this point for $p > 2$, it is the accelerated-electron fraction, ξ_e, rather than γ_m that must evolve. Subscripts in lowercase letters, dn, refer to the properties of the particle distribution, whereas uppercase letters, DN, denote the properties of the bulk outflow. The proper speed of the particle distribution $u_e \equiv \gamma_e\beta_e$ has a subscript 'e' while the proper speed of the outflow $u \equiv \Gamma\beta$ is without this subscript.

In the DN regime, we have

$$\frac{\gamma_{dn}}{G(p)} - 1 \approx \frac{1}{2}\beta_{ud}^2\left(\frac{m_p}{m_e}\right)\epsilon_e\xi^{-1}, \quad \Rightarrow \xi \approx 2.8 \times 10^{-3}\epsilon_{e,-1}^{-1}\tilde{f}(p)\left(\frac{\beta_{ud}}{10^{-2}}\right)^2, \quad (7)$$

where $f(p) \equiv G(p)/[\gamma_{dn} - G(p)] \approx (p-2)/[(\sqrt{2}-1)(p+\sqrt{2})]$ for $p > 2$ and $\gamma_M \to \infty$, and $\tilde{f}(p) \equiv f(p)/f(2.5)$.

For a fixed ϵ_e, the scaling $\xi \propto \beta_{ud}^2$ arises because the shock strength $(\Gamma_{ud} - 1) \approx \frac{1}{2}\beta_{ud}^2$ sets the internal energy per baryon. As the shock weakens, the available energy per electron diminishes. To maintain a power-law distribution with an average LF $\langle\gamma_e\rangle \sim 3\gamma_{dn}$ (e.g., for $p = 2.5$), the energy must be concentrated in a decreasing subset of the electron population, implying a decreasing ξ_{dn}. The critical bulk proper speed u_{DN} at the DN transition can be defined by equating $\xi_{dn} = \xi_{e0}$, leading to

$$u_{DN} \approx \beta_{DN} \approx 0.19\tilde{f}(p)^{-\frac{1}{2}}\xi_{e0}^{\frac{1}{2}}\epsilon_{e,-1}^{-\frac{1}{2}}. \quad (8)$$

For simplicity, throughout this work we assume $\xi_{e0} = 1$. Thus, the scaling of ξ_e across the entire dynamical range is given by

$$\frac{\xi_e}{\xi_{e0}} = \min\left(1, \frac{\beta_{ud}^2}{\beta_{DN}^2}\right) = \begin{cases} 1, & \text{for } \beta_{ud} \geqslant \beta_{DN}, \\ \frac{\beta_{ud}^2}{\beta_{DN}^2}, & \text{for } \beta_{ud} \leqslant \beta_{DN}. \end{cases} \quad (9)$$

In this work, we consider a forward shock propagating into a stationary upstream medium. From this point onward, we therefore drop the subscript *ud* from the outflow velocity.

2.2. Adiabatic Blast-wave Evolution

For illustration purposes, we consider the adiabatic evolution (Appendix B gives the conditions under which adiabatic evolution holds) of a spherical forward blast wave due to single-velocity ejecta launched with u_0 propagating into a cold, stationary external medium characterized by a radial density profile $\rho(R) = AR^{-k}$, where $k = 0$ and 2 correspond to a uniform medium and a stellar wind profile respectively. We will consider synchrotron emission from the shocked fluid.

The dynamics of the shocked fluid are described in terms of the (normalized) proper speed $u \equiv \Gamma\beta$, where Γ is the bulk Lorentz factor and β is the dimensionless velocity in units of c. We assume a spherically symmetric blast wave, with a true kinetic energy E equal to the isotropic-equivalent kinetic energy E_{iso}. In realistic systems such as GRBs, the ultrarelativistic ejecta with $u_0 \gg 1$ are initially *collimated*, and during this phase, the deceleration time is set by the isotropic-equivalent energy E_{iso} rather than the true energy E. For narrow jets, E_{iso} can substantially exceed E. For such collimated outflows, typically within a few dynamical timescales after the jet break, the jet undergoes lateral expansion and gradually transitions toward a quasi-isotropic flow as it becomes subrelativistic (e.g., A. Panaitescu & P. Mészáros 1999; A. Panaitescu & P. Kumar 2000; J. Granot 2007; J. Granot & E. Ramirez-Ruiz 2012). The detailed physics governing this transition are complex and model-dependent. However, once the outflow becomes nonrelativistic, it is already very close to spherical symmetry, and the subsequent hydrodynamics are determined by the true explosion energy E (J. Granot et al. 2005; F. De Colle et al. 2012; J. Granot & T. Piran 2012; P. C. Duffell & T. Laskar 2018). Moreover, beaming corrections to the radiation are at most mild at this stage, such that the we are sensitive to emission from the entire shocked region.

For adiabatic evolution (negligible energy gains or radiative losses), the explosion energy E is approximately constant and both the Blandford–McKee and Sedov–Taylor phase can be

summarized succinctly as

$$M(<R)\, c^2\, u^2(R) = C_u^2 E. \tag{10}$$

Equation (10) captures the correct scaling of the blast-wave evolution, with the factor C_u accounting for the normalization required to recover the exact Blandford–McKee and Sedov–Taylor self-similar solutions. Since these correction factors are of order unity and primarily affect the normalization, we neglect them throughout most of the text for simplicity. The corrected velocity and radius can be obtained by applying the corresponding factors $C_{\rm u}$ and $C_{\rm R}$ (see Appendix C for details).

The swept-up mass depends on the stratification of the external medium, and (for $k < 3$) can be expressed as

$$M(<R) = \int_0^R 4\pi r^2 \rho(r)\, dr = \frac{4\pi A}{3-k} R^{3-k}, \tag{11}$$

which implies

$$u(R) = \sqrt{\frac{(3-k)E}{4\pi A c^2 R^{3-k}}} = u_0 \min\left[1, \left(\frac{R}{R_{\rm dec}}\right)^{-\frac{3-k}{2}}\right], \tag{12}$$

where $R_{\rm dec}$ is the deceleration radius, given by $u(R_{\rm dec}) = u_0$, i.e.,

$$R_{\rm dec} = \left[\frac{(3-k)E}{4\pi A c^2 u_0^2}\right]^{\frac{1}{3-k}}. \tag{13}$$

For nonrelativistic sources like a supernova (SN), the circumstellar medium is wind-like up to a wind termination radius $R_{\rm TS} \lesssim 0.3$ pc (T. J. Moriya 2014; T. Matsuoka et al. 2025) beyond which the density can be assumed to be constant. The proper speed at launch, the ratio of the launch speed to the critical DN proper speed, and the deceleration radius for nonrelativistic sources ($u_0 < u_{\rm DN} \ll 1$) can be expressed as

$$u_0 = \frac{1}{c}\sqrt{\frac{2E}{M_{\rm ej}}} \approx 1.93 \times 10^{-2} E_{51}^{\frac{1}{2}} M_3^{-\frac{1}{2}}, \tag{14}$$

$$\frac{u_0}{u_{\rm DN}} \approx 0.1 \tilde{f}(p)^{\frac{1}{2}} E_{51}^{\frac{1}{2}} M_3^{-\frac{1}{2}} \xi_{\rm e0}^{-\frac{1}{2}} \quad \epsilon_{\rm e,-1}^{\frac{1}{2}}, \tag{15}$$

$$R_{\rm dec} = \left[\frac{3M_{\rm ej}}{8\pi n m_{\rm p}}\right]^{\frac{1}{3}} \approx 2.4 M_3^{\frac{1}{3}}\, n_0^{-\frac{1}{3}}\ {\rm pc}, \tag{16}$$

where $M_3 = M_{\rm ej}/3M_\odot$.

For $u \leqslant 1$, the observed time of emission is given as (see Appendix G for physical motivation)

$$t \approx \frac{2}{5-k}\frac{R}{uc}. \tag{17}$$

At the Newtonian transition time $t_{\rm N}$ we have $u = 1$, and as stated before, the outflow approaches spherical symmetry at this stage. The Newtonian transition occurs at a radius $R_N = R_{\rm dec}(u_0 = 1)$ corresponding to an observed time

$$t_{\rm N} \equiv \frac{2}{5-k}\frac{R_{\rm N}}{c} \approx \begin{cases} 84 E_{51}^{\frac{1}{3}} n_0^{-\frac{1}{3}}\,{\rm days}(k=0), \\ 46 E_{51} A_\star^{-1}\,{\rm days}(k=2). \end{cases} \tag{18}$$

Thus, u evolves in the adiabatic phase as

$$u(t) = \left[\frac{R(t)}{R_{\rm N}}\right]^{-\frac{3-k}{2}} = \begin{cases} \left[\frac{4(4-k)t}{(5-k)^2 t_{\rm N}}\right]^{-\frac{(3-k)}{2(4-k)}} & t \ll t_{\rm N}, \\ \left(\frac{t}{t_{\rm N}}\right)^{-\frac{(3-k)}{(5-k)}} & t \geqslant t_{\rm N}. \end{cases} \tag{19}$$

The DN transition time is (for $u_0 > u_{\rm DN}$)

$$t_{\rm DN} \equiv \frac{2}{5-k}\frac{R_{\rm DN}}{u_{\rm DN} c} \approx \begin{cases} 3.7 E_{51}^{\frac{1}{3}} n_0^{-\frac{1}{3}} \tilde{f}(p)^{\frac{5}{6}} \xi_{\rm e0}^{-\frac{5}{6}} \epsilon_{\rm e,-1}^{\frac{5}{6}}\,{\rm yr}(k=0), \\ 18.7 E_{51} A_\star^{-1} \tilde{f}(p)^{\frac{3}{2}} \xi_{\rm e0}^{-\frac{3}{2}} \epsilon_{\rm e,-1}^{\frac{3}{2}}\,{\rm yr}(k=2). \end{cases} \tag{20}$$

For the ordering $u_0 > 1 > u_{\rm DN}$ we can define the ratio of the Newtonian to the DN transition time as

$$\frac{t_{\rm DN}}{t_{\rm N}} = u_{\rm DN}^{-\frac{5-k}{3-k}} = \left[\frac{f(p)}{2}\frac{m_{\rm p}}{m_{\rm e}}\frac{\epsilon_{\rm e}}{\xi_{e0}}\right]^{\frac{5-k}{2(3-k)}} \approx \begin{cases} 15.7 \tilde{f}(p)^{\frac{5}{6}} \xi_{\rm e0}^{-\frac{5}{6}} \epsilon_{\rm e,-1}^{\frac{5}{6}} (k=0), \\ 143 \tilde{f}(p)^{\frac{3}{2}} \xi_{\rm e0}^{-\frac{3}{2}} \epsilon_{\rm e,-1}^{\frac{3}{2}} (k=2). \end{cases} \tag{21}$$

Equation (21) shows that measuring the ratio of $t_{\rm DN}$ to $t_{\rm N}$ directly constrains $\beta_{\rm DN}$ and the microphysical parameters. This can in principle be measured in GRB afterglows (see Section 3.1).

The swept-up mass of the ambient medium required to transition to the DN regime is

$$M_{\rm DN} \equiv M(<R_{\rm DN}) = \frac{E}{u_{\rm DN}^2 c^2} = \frac{E}{2c^2}\frac{1}{f(p)}\frac{\xi_{\rm e0}}{\epsilon_{\rm e}}\frac{m_{\rm e}}{m_{\rm p}} \approx 1.5 \times 10^{-2} E_{51} \tilde{f}(p)^{-1} \xi_{\rm e0} \epsilon_{\rm e,-1}^{-1} M_\odot, \tag{22}$$

which is independent of the stratification index of the ambient medium k. Physically, this means that the DN regime is realized once the swept-up mass of the ambient medium exceeds a critical mass $M_{\rm DN}$. An outflow decelerates when the swept-up ambient mass becomes comparable to the mass of the ejecta. Therefore, if the ejecta mass satisfies $M_{\rm ej} > M_{\rm DN}$, the outflow enters the DN regime before the deceleration time, i.e., at times $t < t_{\rm dec}$, which is the coasting phase if the outflow is launched at a single velocity. This is typically the case for supernova remnants, whose ejecta masses are on the order of a few $M_\odot$. Kilonova remnants, with characteristic ejecta masses $M_{\rm KNR} \sim 0.1\, M_\odot$, present a particularly interesting scenario. For outflows with $E_{51} \lesssim 1$, the KNR is already in the DN

phase before $t_{\rm dec}$. However, for a magnetar-boosted kilonova remnant with $E_{51} \sim 10$, one obtains $M_{\rm DN} \sim 0.1\, M_\odot$, implying that the DN regime is reached just after deceleration, i.e., at $t_{\rm DN} \gtrsim t_{\rm dec}$ (see Section 3.2). In contrast, GRB jets and magnetar giant flare outflows have ejecta masses far below $M_{\rm DN}$, so their transition to the DN regime occurs only after deceleration, at times $t > t_{\rm dec}$ (see Section 3.1).

The number of electrons in the shocked fluid increases as (for $t \geqslant t_{\rm DN}$)

$$N_{\rm e} \equiv \frac{M(<R)}{m_{\rm p}} = \frac{E}{m_{\rm p}u^2c^2} = \frac{E}{m_{\rm p}u_{\rm DN}^2c^2}\left(\frac{t}{t_{\rm DN}}\right)^{\frac{2(3-k)}{(5-k)}}$$
$$\approx 1.8\times10^{55}\,\tilde{f}(p)\,\epsilon_{\rm e,-1}\,\xi_{\rm e0}^{-1}\times\begin{cases}\left(\frac{t}{t_{\rm DN}}\right)^{\frac{6}{5}}(k=0),\\ \left(\frac{t}{t_{\rm DN}}\right)^{\frac{2}{3}}(k=2).\end{cases} \quad (23)$$

Using Equations (9) and (23), the number of relativistic electrons in the DN phase can be estimated as (for $t \geqslant t_{\rm DN}$)

$$N_{\rm rel} = \xi_{\rm e}N_{\rm e} = \frac{\xi_{\rm e0}E}{m_{\rm p}u_{\rm DN}^2c^2} = \frac{f(p)\epsilon_{\rm e}E}{2m_{\rm e}c^2}$$
$$\approx 1.8\times10^{55}E_{51}\tilde{f}(p)\epsilon_{\rm e,-1}. \quad (24)$$

Equations (23)–(24) show that during the DN phase, although the total number of electrons swept into the shocked fluid increases with time, the number of relativistic electrons stays constant and equals the total number of electrons at the DN transition, so that $N_{\rm rel}$ in Equation (24) can be thought of as the maximum number of electrons accelerated to relativistic velocities in the blast wave. This number is independent of the ambient medium stratification index k. The reason is as follows: in the adiabatic DN regime, relativistic electrons carry a fixed fraction, $\epsilon_e\epsilon_{\rm int}E$ of the outflow energy (where a fraction $\epsilon_{\rm int} \approx \frac{1}{2}$ of the total energy is in internal energy), while maintaining a constant average Lorentz factor to $\langle\gamma\rangle \approx \gamma_{\rm dn}/G(p)$. Thus, since the number of relativistic electrons is the ratio of the two it does not change with time.

Appendix D shows that the slow-cooling synchrotron regime ($\nu_{\rm m} \ll \nu_{\rm c}$) is naturally realized in the DN phase for a broad parameter space. The DN cooling break lies in the optical / UV band (see Equation (D6)). Appendix E shows that, in the DN regime, the self-absorption frequency $\nu_{\rm sa}$ cannot fall below the minimal synchrotron frequency $\nu_{\rm m}$. This is because $\nu_{\rm m}$ lies very close to the cyclotron frequency (within a factor of 2 when $\gamma_{\rm dn} = \sqrt{2}$), making it difficult for $\nu_{\rm sa}$ to reach lower values. Consequently, in the DN phase, the slow-cooling synchrotron spectrum naturally satisfies the ordering $\nu_{\rm m} < \nu_{\rm sa} < \nu_{\rm c}$. In this Spectrum 2 regime (following the terminology of J. Granot & R. Sari 2002), the peak luminosity and corresponding peak frequency are at the self-absorption frequency. The peak/self-absorption frequency (see Appendix H) can be written as (for $t > t_{\rm DN}$)

$$\nu_{\rm pk} = \nu_{\rm sa} = \left[\frac{1}{m_{\rm e}}\frac{L_{\nu,max}}{8\pi^2R^2}\gamma_{\rm dn}^{p-1}\nu_{\rm B}^{\frac{p}{2}}\right]^{\frac{2}{p+4}} \text{ (for } \nu_{\rm sa} > \nu_{\rm m})$$
$$\approx\begin{cases}115E_{51}^{\frac{2}{3(p+4)}}n_0^{\frac{14+3p}{6(p+4)}}\tilde{f}(p)^{-\frac{(2+3p)}{6(p+4)}}\xi_{\rm e0}^{\frac{14+3p}{6(p+4)}}\\ \times\epsilon_{\rm e,-1}^{-\frac{(2+3p)}{6(p+4)}}\epsilon_{\rm B,-2}^{\frac{p+2}{2(p+4)}}t_{0.6}^{-\frac{3p+14}{5(p+4)}}\text{ MHz }(k=0),\\ 12E_{51}^{-1}A_\star^{\frac{14+3p}{2(p+4)}}\tilde{f}(p)^{-\frac{(10+3p)}{2(p+4)}}\xi_{\rm e0}^{\frac{14+3p}{2(p+4)}}\\ \times\epsilon_{\rm e,-1}^{-\frac{(10+3p)}{2(p+4)}}\epsilon_{\rm B,-2}^{\frac{p+2}{2(p+4)}}t_{1.3}^{-\frac{3p+14}{3(p+4)}}\text{ MHz }(k=2),\end{cases} \quad (25)$$

where $t_{0.6} = t/3.7$ yr and $t_{1.3} = t/18.7$ yr. The peak spectral luminosity (see Appendix H) is given as (for $t > t_{\rm DN}$)

$$L_{\rm pk} = L_{\nu_{\rm sa}} = L_{\nu,max}\left(\frac{\nu_{\rm sa}}{\nu_{\rm m}}\right)^{\frac{1-p}{2}} \text{ (for } \nu_{\rm sa} > \nu_{\rm m})$$
$$\approx\begin{cases}7.3\ \times\ 10^{28}E_{51}^{\frac{2p+13}{3(p+4)}}n_0^{\frac{2p+13}{6(p+4)}}\tilde{f}(p)^{\frac{17-2p}{6(p+4)}}\xi_{\rm e0}^{\frac{2p+13}{6(p+4)}}\epsilon_{\rm e,-1}^{\frac{17-2p}{6(p+4)}}\\ \times\epsilon_{\rm B,-2}^{\frac{2p+3}{2(p+4)}}t_{0.6}^{-\frac{(2p+13)}{5(p+4)}}\text{ erg s}^{-1}\text{Hz}^{-1}(k=0)\,,\\ 8\ \times\ 10^{27}A_\star^{\frac{2p+13}{2(p+4)}}\tilde{f}(p)^{-\frac{(3+2p)}{2(p+4)}}\xi_{\rm e0}^{\frac{2p+13}{2(p+4)}}\epsilon_{\rm e,-1}^{-\frac{(3+2p)}{2(p+4)}}\epsilon_{\rm B,-2}^{\frac{2p+3}{2(p+4)}}\\ \times t_{1.3}^{-\frac{(2p+13)}{3(p+4)}}\text{ erg s}^{-1}\text{Hz}^{-1}(k=2).\end{cases} \quad (26)$$

The spectral luminosity at frequency $\nu = \nu_{\rm GHz}$GHz in PLS G ($\nu_{\rm sa} < \nu < \nu_{\rm c}$) of Spectrum 2 following notation by J. Granot & R. Sari (2002) is given as (for $t > t_{\rm DN}$)

$$L_{\nu,\rm G} \equiv L_{\nu_{\rm sa}}\left(\frac{\nu}{\nu_{\rm sa}}\right)^{\frac{(1-p)}{2}} = L_{\nu,max}\left(\frac{\nu}{\nu_{\rm m}}\right)^{\frac{(1-p)}{2}}$$
$$\approx\begin{cases}1.5\ \times\ 10^{28}\,\nu_{\rm GHz}^{\frac{(1-p)}{2}}\,E_{51}\,n_0^{\frac{p+1}{4}}\,\tilde{f}(p)^{\frac{3-p}{4}}\,\xi_{\rm e0}^{\frac{p+1}{4}}\,\epsilon_{\rm e,-1}^{\frac{3-p}{4}}\\ \times\epsilon_{\rm B,-2}^{\frac{p+1}{4}}\,t_{0.6}^{-\frac{3(p+1)}{10}}\text{ erg s}^{-1}\text{Hz}^{-1}\,(k=0)\\ 3\ \times\ 10^{26}\,\nu_{\rm GHz}^{\frac{(1-p)}{2}}\,E_{51}^{\frac{1-p}{2}}\,A_\star^{\frac{3(p+1)}{4}}\,\tilde{f}(p)^{-\frac{(3p-1)}{4}}\xi_{\rm e0}^{\frac{3(p+1)}{4}}\,\epsilon_{\rm e,-1}^{-\frac{(3p-1)}{4}}\\ \times\epsilon_{\rm B,-2}^{\frac{p+1}{4}}\,t_{1.3}^{-\frac{(p+1)}{2}}\text{ erg s}^{-1}\text{Hz}^{-1}\,(k=2)\,.\end{cases} \quad (27)$$

Figure 1 summarizes the temporal evolution of the hydrodynamics, particle microphysics, and synchrotron spectral properties of a spherical blast wave propagating into a constant-density medium. Since the peak of the spectral luminosity L_ν occurs at the synchrotron self-absorption frequency, the most observationally relevant power-law segment (PLS) of the slow-cooling synchrotron spectrum is PLS G ($\nu_{\rm sa} < \nu < \nu_{\rm c}$). This segment extends with a spectral slope $(1-p)/2$ from radio to optical frequencies, and therefore it dominates the observable emission over a broad frequency range.

Table 1 summarizes the temporal decay indices $\alpha_{\rm G}$ (defined as $F_{\nu_{\rm G}} \propto t^{\alpha_{\rm G}}$) in PLS G within the Newtonian and DN regimes

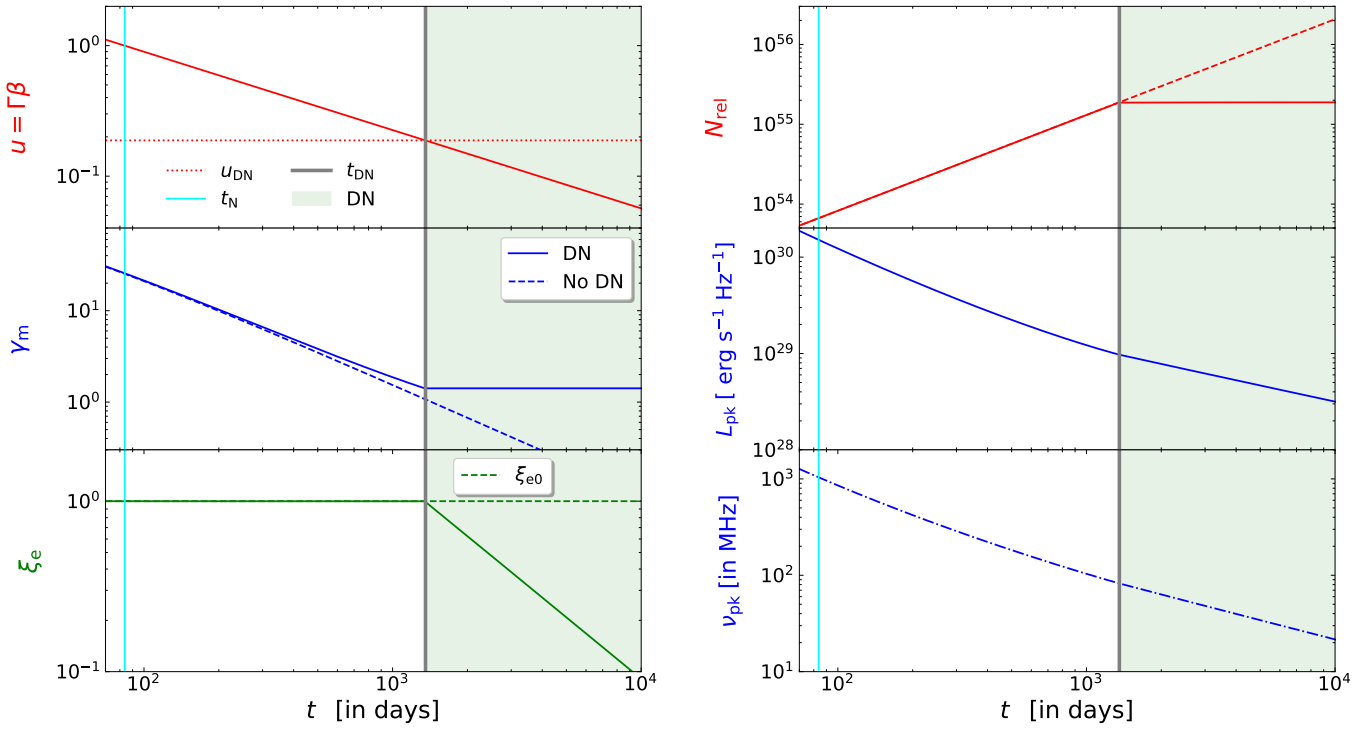


Figure 1. Illustration of the temporal evolution of the hydrodynamics, particle microphysics, and synchrotron spectrum in the DN regime for a spherical blast wave expanding into a constant-density medium for an initially relativistic outflow ($u_0 \gg 1 \Leftrightarrow t_{dec} \ll t_N$). The assumed parameters are $E_{51} = 1$, $n_0 = 1$ ($k = 0$), $\epsilon_e = 0.1$, $p = 2.5$, $\epsilon_B = 0.01$, and $\xi_{e0} = 1$. In both panels, the vertical cyan and gray lines denote the Newtonian transition time (Equation (18)) and the DN transition time (Equation (20)), respectively, while the shaded green region marks the DN regime. Left panel: the top subpanel shows the normalized outflow proper speed u (solid red); the horizontal dashed red line indicates the critical proper speed below which the flow enters the DN regime. The middle subpanel shows the minimum electron Lorentz factor γ_m in solid blue with DN correction, while the dashed blue shows the extrapolation of Equation (5) to Newtonian bulk speed. The bottom subpanel shows the particle acceleration efficiency ξ_e (solid green). Right panel: the top subpanel shows the number of relativistic electrons contributing to the emission (solid red; Equation (24)), while the total number of shocked electrons is shown by the dashed red curve (Equation (23)). The middle and bottom subpanels show the peak luminosity (solid blue; Equation (26)) and corresponding peak frequency (dotted blue; Equation (25)), respectively.

for different orderings of u_0 and u_{DN}, and for an ambient medium characterized by a density stratification index k. An additional quantity of interest is the deviation of the DN temporal slope from the value obtained by extrapolating the Newtonian solution. As an illustration, for $k = 0$ and $t > t_{dec}$, this difference for PLS G is given by

$$\delta\alpha_G \equiv \alpha_{G,DN} - \alpha_{G,N} = \frac{6}{5}(p - 2), \tag{28}$$

which implies that, for $p > 2$, the DN temporal decay is shallower than the extrapolated Newtonian prediction.

In the limit $p \to 2$, Equation (8) indicates that the onset of the DN phase occurs at earlier times as compared with larger p values, while Equation (28) shows that the difference between the DN and Newtonian temporal slopes decreases. However, this limit must be treated with caution, since $\beta_{DN} \to \infty$ as $p \to 2$, and the underlying approximation ceases to be valid. This highlights a trade-off: larger values of p delay the onset of the DN phase through a smaller β_{DN}, but enhance the contrast between the DN and Newtonian temporal slopes, whereas smaller values of p produce the opposite effect.

In this section, we consider an outflow with $u_0 > u_{DN}$. In many astrophysical scenarios like kilonovae and supernovae, the outflow is in the DN phase in the coasting phase itself. The corresponding expressions for these scenarios are summarized in Appendix I.

3. Astrophysical Transients

We turn next to systematically exploring the synchrotron parameter space of astrophysical transients in the DN regime and examining the temporal evolution of the light curves and the spectrum. Our primary objective is to assess the observability of this late-time dynamical phase and identify the physical conditions under which it becomes accessible to current and future radio facilities. Table 2 summarizes the fiducial parameter values adopted for different astrophysical transients.

3.1. Gamma-Ray Burst and Magnetar Giant Flare Afterglow

As an illustrative example of an outflow that is initially highly collimated, later becomes Newtonian, and eventually enters the DN regime, we consider a GRB afterglow in a constant-density medium. By the time the outflow reaches the DN phase, its propagation effectively occurs in a constant-density interstellar medium. Figure 2 shows that, for typical ISM parameters, the DN regime is realized on a timescale of $\sim$ a few years (see Equation (20)), at which point the flux has decayed by roughly 2 orders of magnitude compared to the Newtonian transition, which typically occurs on timescales of $\sim$ a few months (see Equation (18)). As discussed in Equation (28) the DN phase is delayed for large p values, and in that case only nearby sources are expected to be detectable in this phase. The detection prospects improve in a higher-density ambient medium, which both shortens the

Table 1

Temporal Slopes $\alpha_G = \frac{d \ln F_{\nu,G}}{d \ln t}$ in PLS G of the Flux Density $F_{\nu,G} \propto t^{\alpha_G}$ for Different Relative Ordering of (u_0, u_{DN})

Scenario	$t < t_{dec}$	$t_{dec} < t < t_N$	$t_N < t < t_{DN}$	$t > t_{DN}$
$u_0 \gg 1 > u_{DN}$	$3 - \frac{k(p+5)}{4}$	$-\frac{(3-k)(p-1)}{4}$	$-\frac{15p-21-4k(p-2)}{2(5-k)}$	$-\frac{3(p+1)}{2(5-k)}$
$k = 0$	3	$-\frac{3(p-1)}{4}$	$-\frac{3(5p-7)}{10}$	$-\frac{3(p+1)}{10}$
$k = 0$, $p = 2.5$	3	$-\frac{9}{8}$	$-\frac{33}{20}$	$-\frac{21}{20}$
$k = 2$	$-\frac{p-1}{2}$	$-\frac{p-1}{4}$	$-\frac{7p-5}{6}$	$-\frac{p+1}{2}$
$k = 2$, $p = 2.5$	$-\frac{3}{4}$	$-\frac{3}{8}$	$-\frac{25}{12}$	$-\frac{7}{4}$
Scenario	$t < t_{dec}$	$t_{dec} < t < t_{DN}$	$t > t_{DN}$	
$1 > u_0 > u_{DN}$	$3 - \frac{k(p+5)}{4}$	$-\frac{15p-21-4k(p-2)}{2(5-k)}$	$-\frac{3(p+1)}{2(5-k)}$	
$k = 0$	3	$-\frac{3(5p-7)}{10}$	$-\frac{3(p+1)}{10}$	
$k = 0$, $p = 2.5$	3	$-\frac{33}{20}$	$-\frac{21}{20}$	
$k = 2$	$-\frac{p-1}{2}$	$-\frac{7p-5}{6}$	$-\frac{p+1}{2}$	
$k = 2$, $p = 2.5$	$-\frac{3}{4}$	$-\frac{25}{12}$	$-\frac{7}{4}$	
Scenario	$t < t_{dec}$	$t > t_{dec}$		
$u_0 < u_{DN}$	$3 - \frac{k(p+5)}{4}$	$-\frac{3(p+1)}{2(5-k)}$		
$k = 0$	3	$-\frac{3(p+1)}{10}$		
$k = 0$, $p = 2.5$	3	$-\frac{21}{20}$		
$k = 2$	$-\frac{p-1}{2}$	$-\frac{p+1}{2}$		
$k = 2$, $p = 2.5$	$-\frac{3}{4}$	$-\frac{7}{4}$		

Table 2

Fiducial Parameters for Spherical Outflows from Different Astrophysical Transients: M_{ej} and E Refer to the True (Not Isotropic-equivalent) Mass and Kinetic Energy Associated with the Outflow, Respectively, u_{ej} is the Outflow Proper Speed, ϵ_e and ϵ_B Represent the Fractions of Internal Energy Channeled into Shock-accelerated Electrons and Magnetic Field, Respectively in the Shocked External Medium, and ξ_{e0} Represents the Fraction of Number of Nonthermal to Total Electrons in the Pre-DN phase

Object	u_{ej}	M_{ej} [$M_\odot$]	E [erg]	ϵ_e	ϵ_B	ξ_{e0}
Gamma-ray burst (GRB)	$10^2 - 10^3$	$10^{-6} - 10^{-5}$	$10^{50} - 10^{52}$	$10^{-2} - 10^{-0.5}$	$10^{-5} - 10^{-2}$	1
Kilonovae remnant (KNR)	10^{-1}	$10^{-1.5}$	$10^{50.5}$	10^{-1}	10^{-2}	1
Magnetar giant flare (MGF)	$1 - 10^2$	$10^{-11} - 10^{-7}$	10^{45}	10^{-1}	10^{-2}	1
Supernovae remnant (SNR)	$10^{-1.7}$	$10^{0.5}$	10^{51}	10^{-4}–10^{-2}	10^{-3}–10^{-1}	1
Superluminous supernovae (SLSNe)	$10^{-1.2}$	$10^{0.5}$	10^{52}	$10^{-2} - 10^{-1}$	$10^{-3} - 10^{-2}$	1

transition timescale and yields brighter emission. In the DN regime, the flux decay is shallower than what would be inferred by extrapolating from the Newtonian phase. In case such transitions are observed, the ratio of the Newtonian to the DN transition time can be used to constrain shock microphysics (see Equation (21)). This late-time flattening of the decay slope is a universal late-time feature for any outflow evolving in the adiabatic phase (see Table 3).

As another illustrative example of an outflow transitioning to the DN phase, we consider the radio nebula produced from interaction of the 27 December 2004 giant flare from the Galactic magnetar SGR 1806−20 (J. Borkowski et al. 2004; P. B. Cameron et al. 2005; B. M. Gaensler et al. 2005) with a bow-shock shell formed by the magnetar wind interacting with the interstellar medium. This event is of particular interest, as it constitutes the first observational example where the DN regime has been inferred directly from the data (J. Granot et al. 2006). The highest velocity portion (leading edge) of the outflow has an apparent expansion speed of $\beta_{app} \approx 1$ (J. D. Gelfand et al. 2005; G. B. Taylor et al. 2005; G. B. Taylor & J. Granot 2006). Attributing this to its proper speed u implies a true expansion velocity of $\beta \approx 0.7$. The mean apparent speed, measured for this source from radio observations, has a median value of $\langle \beta_{app} \rangle \sim 0.4$ (G. B. Taylor et al. 2005), which is representative speed for the bulk material. The radio nebula powered by this outflow implies a one-sided outflow with an axis ratio of $\sim 2{:}1$. The outflow's expansion speed has been measured to decelerate at $t_{dec} \approx 33$ days, its isotropic-equivalent kinetic energy is inferred to be $E_{k,iso} \sim 10^{46}$erg, and a relatively low ISM density of $n_0 \lesssim 0.3\,\mathrm{cm}^{-3}$ is preferred on energetic grounds (J. Granot et al. 2006). The true outflow energy is inferred to be $E \gtrsim 10^{44.5}$erg. The giant flare outflow collides inelastically with the bow-shock nebula shell, producing initial radio emission from both reverse and forward shocks. After the shock crossing, the outflow enters the adiabatic phase. At the deceleration time, $t_{dec} \approx 33$ days, the radio emission is dominated by a different component attributed to the forward shock going into the external ISM, whose emission peaks at this time and then decays slowly as $F_\nu \propto t^{-1.05 \pm 0.05}$. The emission rapidly transitions to the DN phase, as the deceleration time and DN transition time are nearly coincident, and the flow quickly approaches spherical symmetry upon deceleration. Thus, post-deceleration, the evolution is

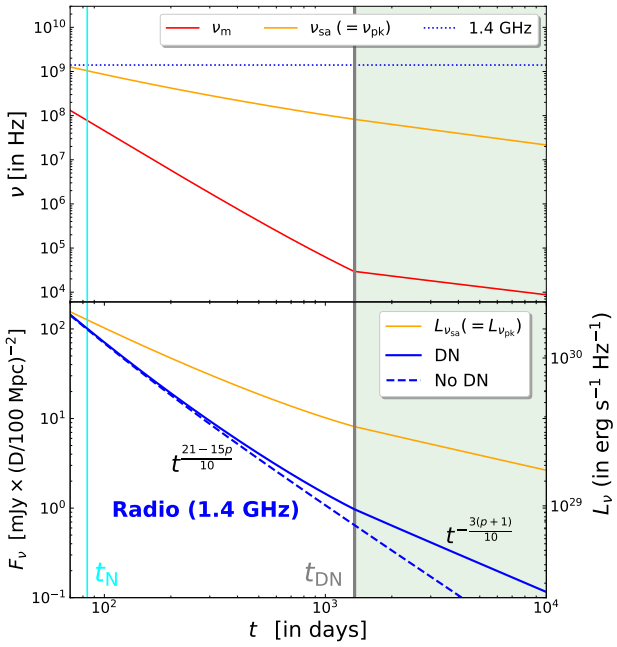


Figure 2. Illustration of the DN phase in a gamma-ray burst radio afterglow for an initially relativistic outflow ($u_0 \gg 1 \Leftrightarrow t_{\rm dec} \ll t_{\rm N}$). The assumed parameters are $E_{51} = 1$, $n_0 = 1$, $\epsilon_e = 10^{-1}$, $p = 2.5$, $\epsilon_B = 10^{-2}$, and $\xi_{e0} = 1$. In all panels, the vertical cyan and gray lines indicate the onset of the Newtonian phase (Equation (18)) and the transition to the DN phase (Equation (20)), respectively. The green shaded region to the right of the gray line denotes the DN regime. In the middle and bottom panels, the flux density (for a source distance of 100 Mpc) is shown on the left y-axis, while the corresponding spectral luminosity is shown on the right (twin) y-axis. Top panel: the temporal evolution of the characteristic synchrotron frequencies, including the minimum frequency $\nu_{\rm m}$ (solid red), the self-absorption frequency $\nu_{\rm sa}$—which also corresponds to the peak frequency in this regime—(solid orange), and the observing frequency $\nu_{\rm obs} = 1.4$ GHz (solid blue). Bottom panel: the peak flux density (left y-axis) and the peak spectral luminosity (right y-axis). For the spectral ordering $\nu_{\rm sa} > \nu_{\rm m}$, the peak occurs at $\nu_{\rm sa}$. The flux density and spectral luminosity at $\nu_{\rm obs} = 1.4$ GHz are shown as functions of time (solid blue). The dashed blue line in the DN regime indicates the extrapolation of the Newtonian-phase temporal slope into the DN phase (see text for details).

determined by the true energy E. For reasonable variations in the true energy of magnetar giant flares, the flux density at the DN transition remains detectable only for Galactic events.

3.2. Kilonova Remnant Afterglow

Simulations of binary neutron star (BNS) mergers indicate a stratified ejecta structure for the kilonova remnant, in which a small fraction of the mass carries most of the kinetic energy (K. Kyutoku et al. 2014; D. Radice et al. 2016; Y. Sekiguchi et al. 2016; M. Shibata & K. Hotokezaka 2019; K. Kawaguchi et al. 2022). We model the outflow using a radially stratified cumulative kinetic energy distribution,

$$E(>u) = E_{\rm tot}\left(\frac{u}{u_{\rm min}}\right)^{-s} \quad \text{for} \quad u_{\rm min} \leqslant u \leqslant u_{\rm max}, \qquad (29)$$

where $E_{\rm tot}$ is the total kinetic energy of the ejecta. Numerical simulations (K. Kyutoku et al. 2014) further suggest that the stratification index s depends on the crustal equation of state and that the high-velocity component ($u \gg 1$) exhibits a flatter slope than the low-velocity component ($u \ll 1$). For concreteness, we focus on the low-velocity regime and adopt $s \simeq 5$.

For simplicity, several previous studies (E. Nakar & T. Piran 2011; S. K. Acharya et al. 2025) have adopted a single-velocity ejecta model. As we show below, ejecta stratification is important primarily during the pre-deceleration phase; after deceleration, in the adiabatic regime, the full ejecta energy has been transferred to the ambient medium. Consequently, the light curves obtained for a single-velocity outflow asymptotically approach those of a stratified ejecta at late times.

The fate of the merger remnant remains uncertain. One possible outcome is the formation of a long-lived millisecond magnetar (B. D. Metzger & A. L. Piro 2014); although observational evidence suggests that, if realized, this should be a rare outcome (P. Beniamini & W. Lu 2021; R. Ricci et al. 2021; H. Wang et al. 2024). If such a long-lived magnetar survives, energy injection during magnetar spin-down can significantly enhance the expansion velocity of the remnant. Following S. K. Acharya et al. (2025), we refer to such a system as an *extreme kilonova remnant* (EKNR), and we explore the resulting multiwavelength light curves in this scenario.

Figure 3 shows the multiwavelength kilonova afterglow light curves for both radially stratified ejecta and single-velocity ejecta. The light curve peaks at the deceleration time, which is the same for both types of ejecta. Differences between the two profiles arise only during the pre-deceleration phase: by the deceleration time, all material in the stratified ejecta has been decelerated, so the full available energy is in the shocked external medium during the adiabatic phase, and the light curves converge. The radially stratified ejecta acts as a gradual energy injection process: faster material decelerates first, followed by slower material, until the deceleration time when even the slowest material has contributed. As each part of the ejecta decelerates, it transfers its energy to the shocked external medium through the pdV work done across the contact discontinuity. Before this time, the single-velocity ejecta, in the coasting phase, show a flux density that grows steeply as t^3, since the number of relativistic electrons scales with the volume ($\propto R^3$) for a uniform external density. This is also the scaling of the energy of the shocked external medium, since the mean energy per particle is constant ($\approx u_0^2 m_p c^2$). In contrast, the stratified outflow exhibits a shallower flux rise and higher flux density due to the continuous energy injection. For KNR, the DN phase begins before deceleration, whereas for EKNR, boosted ejecta speeds delay the DN phase until after deceleration. In both cases, the DN phase typically occurs within a decade; neglecting it and using the standard Newtonian approximation can underestimate the flux density by factors of ∼3–5 in the coasting phase and even larger factors in the post-deceleration phase. Moreover, accounting for the DN phase self-consistently produces a steeper flux rise and a shallower decay. Both of these effects increase the prospects for early detection. All else being equal, the magnetar-boosted EKNR is substantially brighter at all wavelengths, in particular in the radio, improving prospects for detecting such afterglows within a decade following short GRBs. For EKNR, the predicted flux is expected to exhibit a shallow late-time decay once DN effects are included. The existing late-time radio upper limits for the field associated with GW170817 strongly disfavor an EKNR scenario, and by extension, the presence of a long-lived magnetar remnant (see the upper left and right subpanels of Figure 3). More generally,

Table 3
Summary of the Temporal Slopes $\alpha_G = \frac{d \ln F_{\nu,G}}{d \ln t}$ in PLS G for Specific Astrophysical Scenarios in the Newtonian and DN Regimes

Scenario	Object	k	α_G	Relevant Section
$u_0 \gg u_{DN}$	Gamma-ray burst (GRB)	0	$\frac{21-15p}{10}$ for $t_N < t < t_{DN}$ $-\frac{(3p+1)}{10}$ for $t > t_{DN}$	Section 3.1
$u_0 < u_{DN}$	Kilonovae remnant (KNR)	0	$\frac{21+6s-15p}{2(5+s)}$ for $t_N < t < t_{DN}$ $\frac{6s-3(p+1)}{2(5+s)}$ for $t_{DN} < t < t_{dec}$ $-\frac{(3p+1)}{10}$ for $t > t_{DN}$	Section 3.2
$u_0 > u_{DN}$	Extreme kilonovae remnant (EKNR)	0	$\frac{21+6s-15p}{2(5+s)}$ for $t < t_{dec}$ $\frac{21-15p}{10}$ for $t_{dec} < t < t_{DN}$ $-\frac{(3p+1)}{10}$ for $t > t_{DN}$	Section 3.2
$u_0 < u_{DN}$	Radio Supernovae (Pre-deceleration)	2	$\frac{s(1-p)-3(1+p)}{2(s+3)}$ for $t < t_{dec}$	Section 3.3
$u_0 < u_{DN}$	Superluminous Supernovae (SLSNe)	0	$\frac{21+6s-15p}{2(5+s)}$ for $t < t_{DN}$ $\frac{6s-3(p+1)}{2(5+s)}$ for $t_{DN} < t < t_{dec}$ $-\frac{(3p+1)}{10}$ for $t > t_{DN}$	Section 3.3

Note. Here, s denotes the power-law index of the cumulative energy profile of the ejecta (see Equation (29)), k is the stratification index of the ambient medium, and p is the power-law index of the nonthermal electron energy distribution. The expressions for the single-velocity ejecta case can be obtained in the limit $s \to \infty$.

the predicted shallow late-time decay in such systems motivates continued radio monitoring of future nearby short GRB sources down to sensitivities of order μJy, both to detect EKNRs if they exist and to constrain the BNS merger driven magnetar formation rate.

3.3. Early Radio Light Curves of Supernovae

In this section, we examine the influence of the DN phase on the pre-deceleration light curves of supernova remnants. For illustrative purposes, we consider two representative cases: (i) superluminous supernovae (SLSN) remnant expanding into a constant-density medium ($k = 0$), and (ii) typical core-collapse supernovae (CCSNe) evolving in a wind-stratified environment ($k = 2$).

The assumption of a constant-density ambient medium for SLSNe is motivated as follows. Only a small number of SLSNe have been detected in the radio band at early times. Recent observational studies aimed at detecting radio emission from SLSNe (e.g., T. Eftekhari et al. 2021) adopt this simplifying assumption in order to place constraints on the circumburst density in the largely nondetection-dominated sample.

Equation (15) shows that supernova remnants remain in the DN phase from the outset. The wind-like environment typically continues up to a termination shock at $R \lesssim 0.3$ pc, beyond which the ambient medium can be assumed to have a constant density. The deceleration essentially happens in a constant-density medium. For SNe with $u_0 \ll 1$, the deceleration time is given as

$$t_{dec} = \frac{2}{5-k}\frac{R_{dec}}{u_0 c} \approx 165 E_{51}^{-\frac{1}{2}} M_3^{-\frac{1}{6}} n_0^{-\frac{1}{3}} \mathrm{yr}. \quad (30)$$

The peak frequency is given as (see Appendix I)

$$\nu_{pk} = \nu_{sa} \text{ for } t < t_{dec} \approx \begin{cases} 6.4 \times 10^5 \tilde{f}(p)^{\frac{2}{p+4}} n_0^{\frac{6+p}{2(p+4)}} \\ \times \epsilon_{e,-1}^{\frac{2}{p+4}} \epsilon_{B,-2}^{\frac{2+p}{2(p+4)}} \left(\frac{E_{51}}{M_3}\right)^{\frac{8+p}{2(p+4)}} t_{100}^{\frac{2}{p+4}} \mathrm{Hz} (k=0), \\ 4 \times 10^8 \tilde{f}(p)^{\frac{2}{p+4}} A_\star^{\frac{6+p}{2(p+4)}} \\ \times \epsilon_{e,-1}^{\frac{2}{p+4}} \epsilon_{B,-2}^{\frac{2+p}{2(p+4)}} \left(\frac{E_{51}}{M_3}\right)^{\frac{1}{p+4}} t_{100}^{-1} \mathrm{Hz} (k=2), \end{cases} \quad (31)$$

while the peak spectral luminosity (see Appendix I) is given as

$$L_{pk} = L_{\nu_{sa}} \text{ for } t < t_{dec} \approx \begin{cases} 1.5 \times 10^{19} \quad \tilde{f}(p)^{\frac{5}{p+4}} n_0^{\frac{2p+13}{2(p+4)}} \epsilon_{e,-1}^{\frac{5}{p+4}} \\ \times \epsilon_{B,-2}^{\frac{2p+3}{2(p+4)}} \left(\frac{E_{51}}{M_3}\right)^{\frac{2p+13}{p+4}} t_{100}^{\frac{2p+13}{p+4}} \frac{\mathrm{erg}}{\mathrm{s\,Hz}} (k=0), \\ 1.6 \times 10^{25} \tilde{f}(p)^{\frac{5}{p+4}} A_\star^{\frac{2p+13}{2(p+4)}} \epsilon_{e,-1}^{\frac{5}{p+4}} \\ \times \epsilon_{B,-2}^{\frac{2p+3}{2(p+4)}} \left(\frac{E_{51}}{M_3}\right)^{\frac{2p+13}{2(p+4)}} \frac{\mathrm{erg}}{\mathrm{s\,Hz}} (k=2), \end{cases} \quad (32)$$

where $t_{100} = t/100$days.

Similar to KNR, the SNR can also have a radially stratified velocity distribution. We derive an expression for the cumulative energy stratification index s for supernova ejecta in Appendix J.

Figure 4 shows the temporal evolution of the peak luminosity and corresponding peak frequency. For CCSNe in a wind-like medium, the decay of the self-absorption

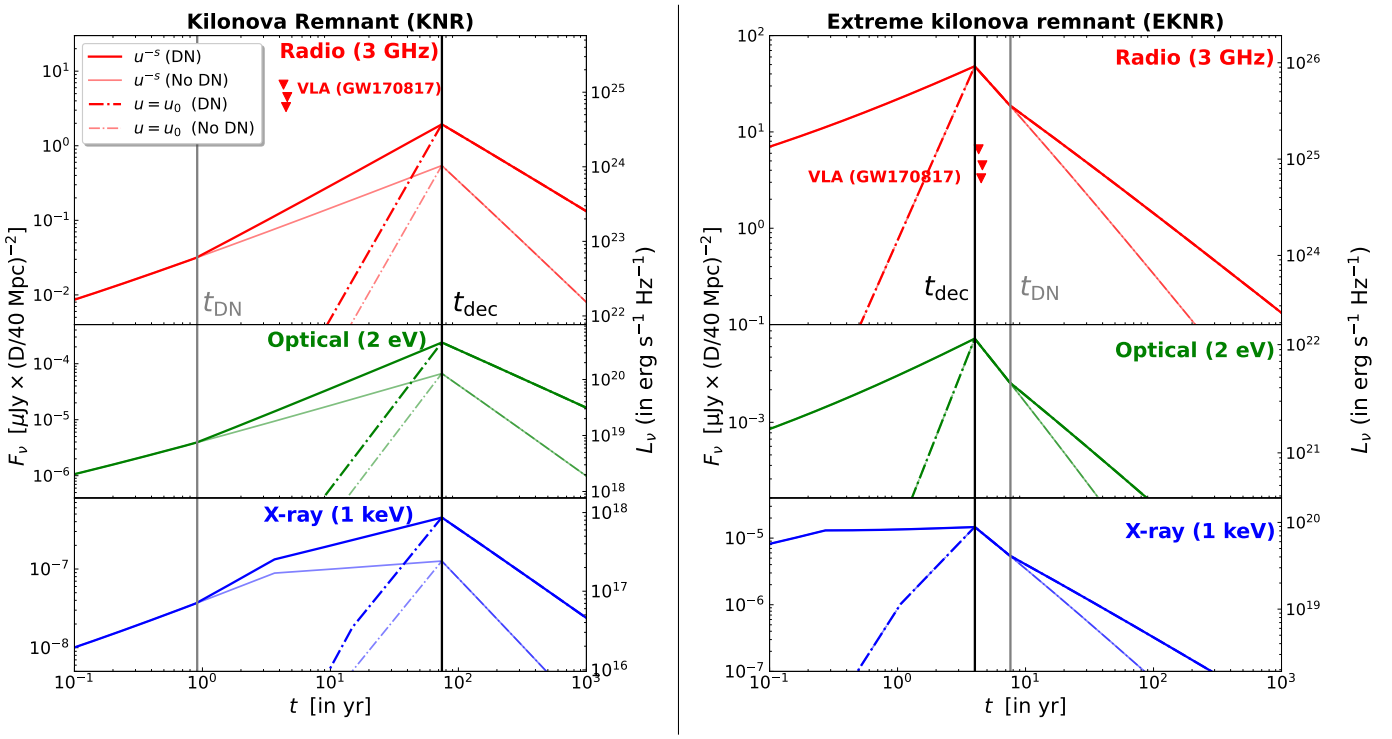


Figure 3. Impact of DN phase on multiwavelength afterglow from a kilonova remnant (KNR; left) and a magnetar-boosted extreme kilonova remnant (EKNR; right) at $D = 40$ Mpc. Both panels assume $\epsilon_e = 0.1$, $\epsilon_B = 0.01$, $p = 2.5$, and $\xi_{e0} = 1$, giving a critical proper speed $u_{DN} \approx 0.2$. An ambient number density $n_0 = 0.01$ cm^{-3} is assumed. Stratified ejecta use $s = 5$, with $u_{0,max} = 1.2$ and $u_{0,min}$ equal to the launch velocity of the single-velocity ejecta $u_0 = \sqrt{\frac{2E_0}{M_{ej}c^2}} \approx 0.06$ (KNR) and 0.3 (EKNR). The ejecta mass is $M_{ej} = 0.1\ M_\odot$, with total kinetic energy $E_0 = 10^{50.5}$ erg (KNR) and 10^{52} erg (EKNR). The radio upper limits for the field associated with GW170817 in the upper left and right subpanels are taken from A. Balasubramanian et al. (2022). Solid lines show stratified ejecta; dotted–dashed lines show single-velocity ejecta. Thick lines include the DN phase; thin lines use the Newtonian approximation. Left y-axis shows flux density F_ν (μJy); right y-axis shows spectral luminosity L_ν (erg s^{-1} Hz^{-1}). Gray and black vertical lines mark the DN transition and deceleration time, respectively; the cyan line (right panel) marks the Newtonian transition for EKNR. Top, middle, and bottom panels show radio (3 GHz), optical (2 eV; r-band), and X-ray (1 keV) light curves in red, green, and blue. For identical microphysics and distance, EKNR is significantly brighter across all bands (see text for details).

frequency (equivalent to the peak frequency for Spectrum 2) is very steep, shifting from tens of GHz to hundreds of MHz within days. The observed luminosity in a given radio band peaks when the self-absorption frequency passes through it. Equation (32) shows that, during the coasting phase in a wind-like external medium the peak luminosity remains constant, while Equation (31) indicates that the peak frequency scales as t^{-1} (see Appendix I for derivation). This behavior can be understood physically as follows. In a wind-like medium, the number of radiating relativistic electrons scales as $N_{rel} \propto R$, whereas the post-shock magnetic field scales as $B \propto R^{-1}$. Consequently, the maximum spectral luminosity is constant, $L_{\nu,max} \propto N_{rel} B \propto R^0$. In addition, both the characteristic synchrotron frequency ν_m and the peak (self-absorption) frequency ν_{sa} scale as ν_m, $\nu_{sa} \propto R^{-1}$. Therefore, the peak luminosity, $L_{pk} = L_{\nu,max}\left(\frac{\nu_{pk}}{\nu_m}\right)^{(1-p)/2} \propto R^0$, is also a constant, while the peak frequency decreases as $\nu_{pk} \propto R^{-1} \propto t^{-1}$. The rise and decay of the flux are determined solely by the relative location of the observing band with respect to the self-absorption frequency. For the first ∼100 days, light curves are nearly identical, whether the DN phase is accounted for or the Newtonian approximation is used; differences emerge at later times. Both stratified and single-velocity ejecta show similar behavior, though the stratified profile yields brighter emission. A combination of single-velocity and stratified ejecta can reproduce the observed spread in peak times and peak luminosities in the 2–10 GHz band (M. F. Bietenholz et al. 2021).

The lower left panel illustrates an application to the nearby CCSN SN 2023ixf (A. J. Nayana et al. 2025). Assuming single-velocity ejecta, the time dependence of the peak frequency can be removed, and the peak flux is expressed as a function of peak frequency. Using $p = 2\alpha + 1$ (where α is the spectral slope in $F_\nu \propto \nu^{-\alpha}$) from the PLS G, the stratification index k can then be fitted assuming single-velocity ejecta. The best-fit value, $k = 1.29 \pm 0.14(2\sigma)$, is in excellent agreement with the constraints of free–free absorption (A. J. Nayana et al. 2025). The upper right panel shows that, for SLSNe in a constant-density medium, the peak frequency remains near ∼100 MHz, making the low-frequency radio bands at LOFAR the most promising for late-time radio detections from SLSN sites. By comparison, the peak luminosity at GHz frequencies is nearly an order of magnitude lower. The lower right panel shows that deeper radio nondetections at GHz frequencies (T. Eftekhari et al. 2021) can place upper limits on the ambient number density, assuming fixed supernova energy and ejecta mass. The lower right panel shows that a higher number density corresponds to a shorter deceleration time, predicting a higher flux at the same observing band at later times. Continued observations are recommended in order to test this prediction.

In the supernova literature, several prescriptions have been adopted for the minimum electron Lorentz factor, γ_m. One

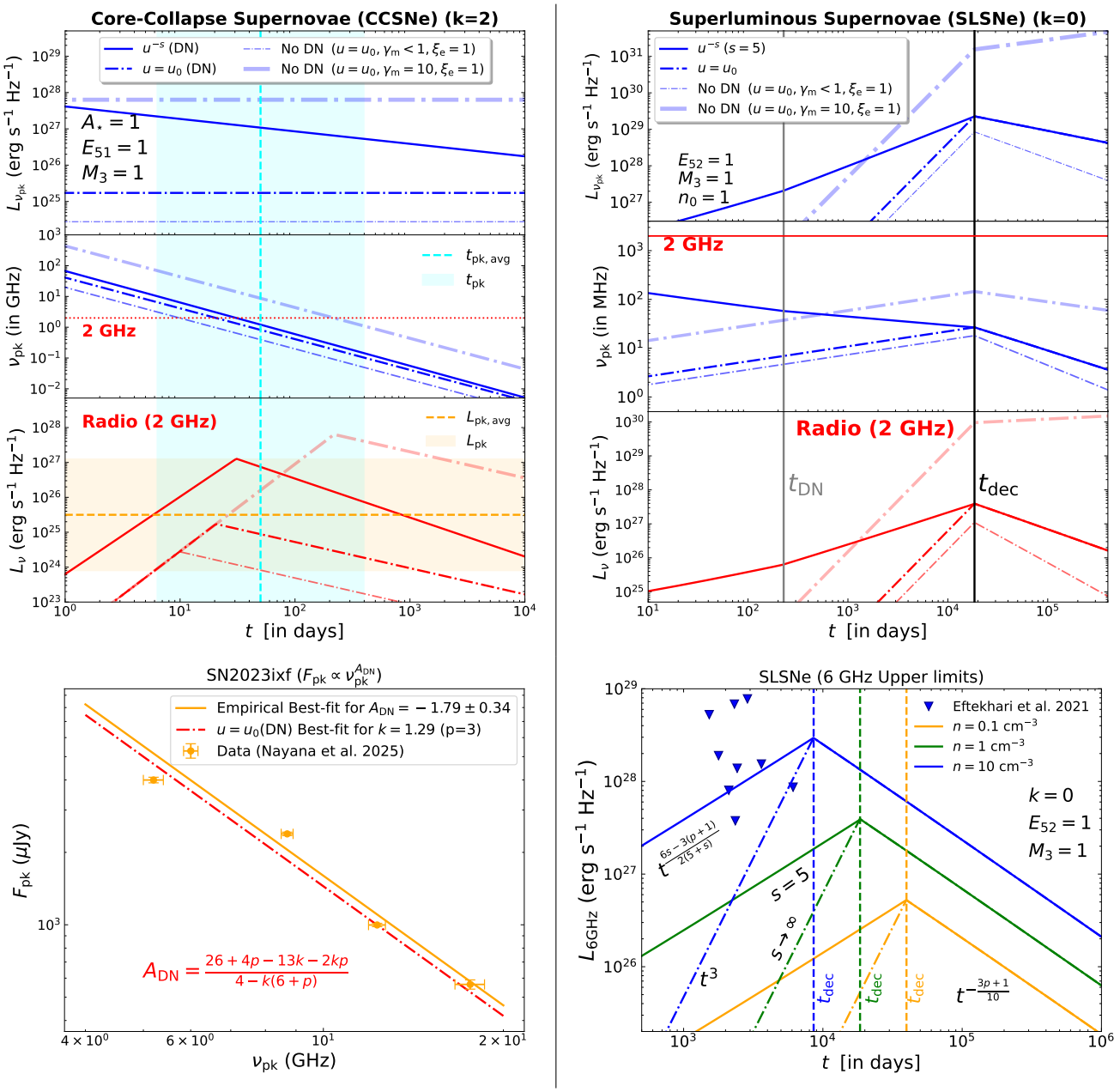


Figure 4. Illustration of the DN phase on early radio light curves for core-collapse supernovae (CCSNe; left) and superluminous supernovae (SLSNe; right). Both upper panels show the peak spectral luminosity (top subpanel, blue), the corresponding peak frequency (middle subpanel, blue), and the spectral luminosity at 2 GHz (bottom subpanel, red). As in Figure 3, solid lines correspond to a radially stratified ejecta at launch with stratification index $s = 5$, while dotted–dashed lines indicate single-velocity ejecta. In both panels, the thicker dotted–dashed lines in lighter shades correspond to fixing $\gamma_m = 10$ with $\xi_e = 1$, and the narrower dotted–dashed lines in lighter shade correspond to Newtonian extrapolation (Equation (6)) with $\xi_e = 1$. The microphysical parameters are $\epsilon_e = 0.1$, $\epsilon_B = 0.01$, $p = 2.5$, and $\xi_{e0} = 1$, giving a critical proper speed $u_{DN} \approx 0.2$. The total energies are (E_{SN}, M_{SNR}) = (10^{51}erg, $3M_\odot$) for CCSNe and (10^{52}erg, $3M_\odot$) for SLSNe. The CCSNe expansion assumes a wind-like medium ($k = 2$) with $A_\star = 1$, whereas the SLSNe assume a uniform-density medium with $n_0 = 1$ cm^{-3}. Left panels: left Upper panel: The vertical cyan dotted line marks the average observed radio peak time of CCSNe, $t_{pk,avg} = 10^{1.7}$ days, while the cyan band indicates the observed range, $t_{pk} = 10^{0.8}$–$10^{2.6}$ days, in the 2–10 GHz radio band. Horizontal dashed orange lines indicate the average observed peak luminosity $L_{pk} = 10^{25.5}$ erg s^{-1} Hz^{-1}, and the orange band shows its spread $L_{pk} = 10^{23.9} - 10^{27.1}$ erg s^{-1} Hz^{-1} (M. F. Bietenholz et al. 2021). The middle subpanel shows the temporal evolution of the peak evolution, while the bottom subpanel shows the 2 GHz light curves. Lower left panel: best-fit value for ambient medium stratification $k = 1.29$ of the nearby CCSN SN 2023xif based on F_{pk}–ν_{pk} data (A. J. Nayana et al. 2025) and the corresponding DN fit using $p = 3$ as inferred from optically thin spectra. Upper right panel: gray and black vertical lines mark the DN transition time and deceleration time for the radial outflow. The temporal slopes in the bottom subpanel are summarized in Table 3. Lower right panel: constraints on the constant ISM density n_0 for SLSNe from 6 GHz upper limits (T. Eftekhari et al. 2021), assuming (E_{SN}, M_{SNR}) = (10^{52}erg, $3M_\odot$). The dotted–dashed lines correspond to single-velocity ejecta, while the solid lines correspond to radially stratified ejecta with stratification index $s = 5$. Both curves merge at $t = t_{dec}$ (shown as vertical dashed lines). The orange, green, and blue curves correspond to radio light curves at 6 GHz for ambient particle densities $n = (0.1, 1, 10)$ cm^{-3}. The time axis is not extended beyond the regime where the adiabatic approximation breaks down, as detailed in Appendix B (see text for more details).

common approach is to use the Newtonian limit of the standard relativistic expression while assuming that all electrons are accelerated ($\xi_e = 1$) (A. M. Soderberg et al. 2005; R. A. Chevalier & C. Fransson 2006; A. Kamble et al. 2014). However, this prescription yields $\gamma_m < 1$, which is unphysical. Moreover, in the Newtonian limit, this prescription

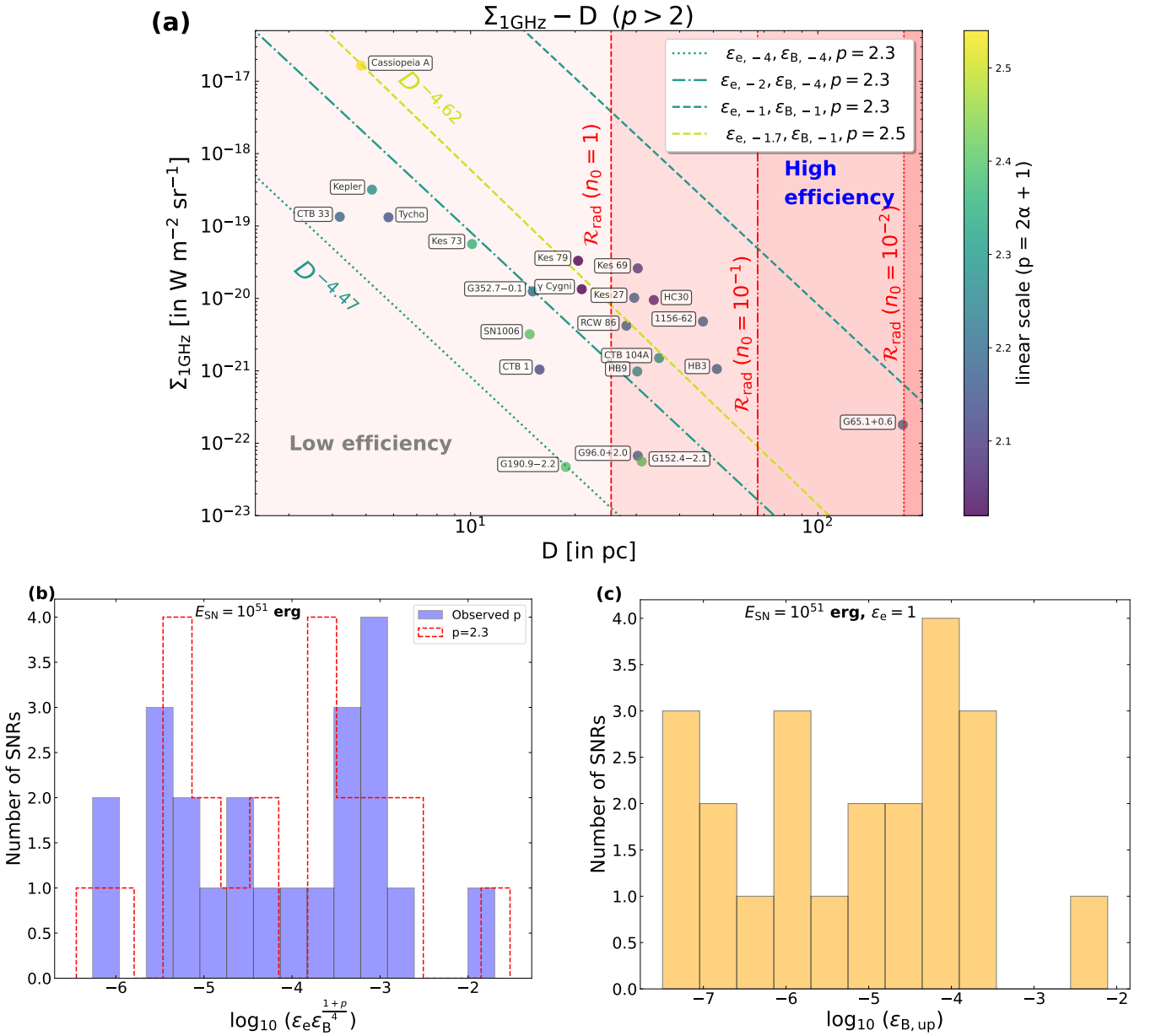


Figure 5. Illustration of the DN phase on the radio surface brightness–diameter (Σ–D) relation of evolved galactic SNRs. For all panels, a uniform ambient medium with stratification index $k = 0$ and an explosion energy of $E_{SN} = 10^{51}$ erg is assumed. Upper panel (a): the Σ–D relation at 1 GHz is shown for 22 Galactic SNRs with power-law index $p > 2$ (see Table K1). Data points are color-coded by their inferred p value, with the linear color scale shown on the right. The common names of individual remnants are labeled. The vertical dashed, dotted–dashed, and dotted red lines mark the transition radii $\mathcal{R}_{rad} = (25.4,\ 67.1,\ 177.0)$ pc, beyond which adiabatic evolution transitions to the radiative phase, for ambient densities $n_0 = (1,\ 10^{-1},\ 10^{-2})$, respectively (see Appendix B). The red shaded regions (lighter on the left and darker on the right) denote the radiative phase for intermediate ambient densities. Model DN curves are shown for different combinations of (ϵ_e, ϵ_B, p), as indicated in the legend. For a given value of p, very low values of (ϵ_e, ϵ_B) are required to span the lower left corner of the plot, whereas higher values populate the upper right region. The deep green and greenish-yellow lines correspond to $p = (2.3, 2.5)$, respectively, consistent with the color-coded colormap. Panel (b) shows the histogram of the parameter combination $\epsilon_e\ \epsilon_B^{\frac{1+p}{4}}$ assuming a fixed explosion energy of $E_{SN} = 10^{51}$ erg. Panel (c) shows the histogram of the upper limit on ϵ_B, which shows a distribution of ϵ_B that is several orders of magnitude wide (see text for discussion).

implies $\gamma_m - 1 \propto \beta^2$, leading to a minimal synchrotron frequency $\nu_m \propto \beta^5$. This steep velocity dependence propagates into the determination of the synchrotron self-absorption frequency and other inferred source properties. The use of this prescription is not unique to supernova studies, and it has also been adopted in several kilonova radio-emission models (T. Piran et al. 2013; G. Sadeh et al. 2024).

Alternatively, some studies (S. P. Reynolds 1998; S. P. Reynolds et al. 2021) adopt a fixed value, typically $\gamma_m = 10$, while assuming different prescriptions for the accelerated-electron fraction, such as $\xi_e = 1$, $\xi_e \propto \beta$, or $\xi_e \propto \beta^2$. While fixing γ_m avoids the problem of $\gamma_m < 1$, not all choices of ξ_e are physically consistent. In Newtonian shocks, maintaining a fixed relativistic γ_m requires $\xi_e \propto \beta^2$. In particular, adopting $\xi_e = 1$ and $\gamma_m = 10$ leads to a significant overprediction of the radio flux. Consequently, many commonly adopted prescriptions either underpredict or overpredict the radio flux (see the upper panels of Figure 4).

Other treatments (R. A. Chevalier & C. Fransson 2006) parameterize the relativistic electron population by assuming that its energy density scales with the post-shock internal energy density while adopting $\gamma_m = 1$. Although this approach is more closely related to the DN framework, it leaves ξ_e unspecified.

We emphasize that γ_m should not be regarded as an independent free parameter. For a given shock velocity and set of microphysical parameters, γ_m is a derived quantity. Only when the formal Newtonian expression predicts $\gamma_m < 1$ does this extrapolation cease to be physically meaningful. At this point, one naturally transitions to the DN regime, in which γ_m is fixed at a mildly relativistic value and ξ_e is determined self-consistently from energy conservation.

3.4. Σ–D Relation in Evolved Supernova Remnants

In this subsection, we explore the radio surface brightness–diameter relationship (Σ–D) for evolved and extended Galactic SNR (see Appendix K for a derivation). In core-collapse scenarios, the SNR reaches the deceleration phase in an effectively constant-density medium (since the total mass of the stellar wind, let alone its unshocked part, is not expected to exceed that of the SN ejecta). Moreover, the typical deceleration radius is $R_{\rm dec} \approx 2.4$ pc (see Equation (16)), supporting the use of a uniform-density profile ($k = 0$) when examining the relation Σ—D for typical diameters $D \gtrsim 5$ pc. Since in this work we focus on the adiabatic evolution, for the extended SNR sample considered in this section we explicitly indicate the transition radius beyond which this approximation breaks down and the SNR enters the radiative phase (see Appendix B).

For the typical range of $\epsilon_e \approx 10^{-4} - 10^{-2}$ and $\epsilon_B \approx 10^{-3} - 10^{-1}$ assumed in extended SNRs (S. P. Reynolds et al. 2021), the $\Sigma - D$ relation in PLS G at $\nu = 1$ GHz can be written as (see Appendix K) (for $p = 2.3$ and $k = 0$)

$$\Sigma_{1\rm GHz} \approx 7.4\times\ 10^{-20} \epsilon_{e,-2}\, \epsilon_{B,-3}^{\frac{1+p}{4}} E_{51}^{\frac{p+5}{4}} D_{10}^{-\frac{(3p+11)}{4}} \frac{\rm W}{\rm m^2\ Hz\ Sr}\ , \tag{33}$$

where $D_{10} = D/(10\,{\rm pc})$.

Figure 5 shows the relation of radio surface brightness (at 1 GHz) to diameter for 22 Galactic supernova remnants with $p > 2$ (see Table K1). Using the $p = 2\alpha + 1$ derived from the optically thin spectral index, we remove p as a free parameter. For a fixed value of $p = 2.3$ and $E_{\rm SN} = 10^{51}$ erg, it can be seen that a very large range of (ϵ_e, ϵ_B) must be spanned in order to explain the large scatter in the data. Furthermore, for fixed (ϵ_e, ϵ_B), different values of p correspond to different scalings of the surface brightness with diameter. For $p = (2.1, 2.3, 2.5)$, the surface brightness scales as $D^{-4.32}$, $D^{-4.47}$, and $D^{-4.62}$, respectively. This illustrates why the exponent obtained from the empirical fits may be less representative of the general population, as a wide variation in (ϵ_e, ϵ_B, p) is required to account for the full spread of the observed data. Due to the steep dependence of the surface brightness on diameter, higher values of (ϵ_e, ϵ_B) are required in order to explain the surface brightness of SNRs with larger diameters (indicating very efficient particle acceleration and post-shock magnetic field amplification), while lower values are required for remnants with smaller diameters (indicating less efficient particle acceleration and post-shock magnetic field amplification). The lower panels demonstrate that, for a fixed explosion energy $E_{\rm SN} = 10^{51}$ erg, the combination $\epsilon_e\, \epsilon_B^{\frac{1+p}{4}}$ can be directly constrained and exhibits a broad scatter spanning several orders of magnitude. By taking $\epsilon_e = 1$ (the maximum physical value), one obtains an upper bound on ϵ_B, which likewise extends over several orders of magnitude. Such a wide range naturally translates into significant dispersion in the predicted synchrotron surface brightness, thereby contributing to the large scatter observed in the Σ–D relation.

While this analysis assumes a fixed supernova energy, realistic explosions are expected to exhibit a spread in $E_{\rm SN}$ of up to an order of magnitude. However, this variation is subdominant compared to the much broader distribution inferred for the microphysical parameters. We therefore conclude that the dominant source of the observed scatter in the surface brightness–diameter relation is the intrinsic diversity in the microphysical parameters, rather than variations in the explosion energy.

4. Conclusion

The deep Newtonian phase represents a generic stage in the late-time evolution of astrophysical outflows, corresponding to the onset of a quasi-spherical Newtonian blast-wave. In this regime, the power-law relativistic electron population responsible for the synchrotron emission starts at mildly relativistic energies and the emission typically occurs in the slow-cooling, self-absorbed synchrotron regime ($\nu_m < \nu_{\rm sa} < \nu_c$), with the flux density peaking at the self-absorption frequency, $\nu_{\rm sa}$, usually in the sub-GHz band. Low-frequency radio observations therefore provide the most direct probe of this phase.

For outflows launched with ultrarelativistic or mildly relativistic velocities, such as GRB jets and magnetar giant flares, the transition to the DN regime occurs after the deceleration phase. By contrast, for supernova and kilonova ejecta, the DN regime is already established during the coasting phase. The essential difference between the standard Newtonian approximation and the DN regime lies in the scaling of the characteristic synchrotron frequency: $\nu_{\rm m} \propto \beta^5 \propto t^{-3}$ in the former, whereas $\nu_{\rm m} \propto \beta \propto t^{-3/5}$ in the latter. Neglecting the DN phase can lead to a significant underestimate of the radio flux, by factors of ~5–6 during the coasting phase and by even larger factors after deceleration. Moreover, the temporal slopes of the light curve are modified, with a steeper flux rise and a shallower decay in the DN regime compared to the standard Newtonian case (see Equation (28)).

Late-time, low-frequency radio observations of a broad class of astrophysical transients are therefore strongly motivated. Even nondetections can place meaningful constraints on the outflow energetics and the density of the surrounding medium.

In the DN phase, the synchrotron self-absorption frequency, which traces the spectral peak, is typically found at low radio frequencies (~100 MHz–1 GHz). Instruments such as LOFAR (M. P. van Haarlem et al. 2013) and SKA (A. Weltman et al. 2020) are therefore well suited to probe this regime. For characteristic outflow energies of $E \sim 10^{51}$ erg and flux sensitivities of order ~10 μJy, this transition may be detectable in GRB afterglows within a decade for nearby events within a few hundred Mpc.

For magnetar giant flares, this phase is likely observable only for nearby Galactic events. In the case of supernovae, there is no sharp transition, as the DN phase is effectively

reached during the coasting phase; for nearby events, tracking the spectral peak evolution can provide a useful probe of the ambient density stratification. For superluminous supernovae, even radio nondetections can place stringent limits on the ambient density. Finally, for nearby short GRBs, the absence of a radio kilonova signal can constrain the presence and properties of a long-lived central magnetar engine.

Acknowledgments

S.M.R. and J.G. thank the Yukawa Institute for Theoretical Physics at Kyoto University, where this work was nearly completed during the YITP long-term workshop YITP-T-26-02 on "Multi-Messenger Astrophysics in the Dynamic Universe." S.M.R. acknowledges useful discussions with A. J. Nayana. P.B. is supported by a grant (no. 2024788) from the United States-Israel Binational Science Foundation (BSF), Jerusalem, Israel, by a grant (no. 1649/23) from the Israel Science Foundation, and by a grant (no. 80NSSC 24K0770) from the NASA Astrophysics Theory Program.

Appendix A
Illustration of the DN Phase from Power-law Distribution in Particle Momenta

In this appendix, we consider a power-law distribution in the proper speed u_e of the nonthermal particles:

$$\frac{dN}{du_e} = K\, u_e^{-p}, \quad u_e = \sqrt{\gamma_e^2 - 1}\,, \tag{A1}$$

where K is a normalization constant.

Following L. Sironi & D. Giannios (2013) we define,

$$x = \gamma_e - 1 \quad \Rightarrow \quad u_e = \sqrt{(x+1)^2 - 1} = \sqrt{2x + x^2}. \tag{A2}$$

The distribution in x is obtained via

$$\frac{dN}{dx} = \frac{dN}{du_e}\frac{du_e}{dx}. \tag{A3}$$

Next, we compute the derivative:

$$\frac{du_e}{dx} = \frac{d}{dx}\sqrt{2x + x^2} = \frac{1+x}{\sqrt{2x + x^2}}. \tag{A4}$$

Thus, the distribution in x becomes

$$\begin{aligned}\frac{dN}{dx} &= K\,(2x + x^2)^{-\frac{p}{2}} \cdot \frac{1+x}{\sqrt{2x + x^2}} \\ &= K(1+x)(2+x)^{-\frac{p+1}{2}} x^{-\frac{p+1}{2}} \\ &\approx \begin{cases} Kx^{-p} \text{ for } & x \gg 1, \\ K(2x)^{-\frac{p+1}{2}} \text{ for } & x \ll 1. \end{cases}\end{aligned} \tag{A5}$$

The number of nonthermal electrons scales as

$$\begin{aligned}N(x) \sim x\frac{dN}{dx} &= K(1+x)(2+x)^{-\frac{p+1}{2}} x^{\frac{1-p}{2}} \\ &\propto \begin{cases} x^{1-p} \text{ for } & x \gg 1, \\ x^{\frac{1-p}{2}} \text{ for } & x \ll 1 \end{cases},\end{aligned} \tag{A6}$$

while the energy of the nonthermal electrons scales as

$$\begin{aligned}E(x) \sim x^2\frac{dN}{dx} &= K(1+x)(2+x)^{-\frac{p+1}{2}} x^{\frac{3-p}{2}} \\ &\propto \begin{cases} x^{2-p} \text{ for } & x \gg 1, \\ x^{\frac{3-p}{2}} \text{ for } & x \ll 1 \end{cases},\end{aligned} \tag{A7}$$

and peaks at the value

$$x_{pk} = \frac{3 - p + \sqrt{3-p}}{p-2} \quad \text{for } 3 < p < 2\,. \tag{A8}$$

Figure A1 and Equation (A5) show that, for $u_{e,min} < 1$, the total number of particles is dominated by those near $u_{e,min}$. However, as expressed in Equation (A8), the energy distribution peaks at $x_{pk} > x_{min}$, implying that, while most particles reside at low energies, the bulk of the energy is carried by higher-energy mildly relativistic particles. As shown on the right panels no such feature exists if a power-law distribution is assumed in $(\gamma_e - 1)$.

It is instructive to consider the number and kinetic-energy fractions above $\gamma_{dn} = \sqrt{2}$ ($u_{dn} = 1$), defined as

$$\begin{aligned}\xi_e &\equiv \xi_{e,pl}(>\gamma_{dn}) = \frac{N(>\gamma_{dn})}{N_{total}}, \\ \epsilon_e &\equiv \epsilon_{e,pl}(>\gamma_{dn}) = \frac{E(>\gamma_{dn})}{E_{total}}.\end{aligned} \tag{A9}$$

where $\xi_{e,pl}$ and $\epsilon_{e,pl}$ are the number and energy fraction for the full distribution functions for both prescriptions.

We compare power laws defined in kinetic energy, $x = \gamma - 1$, and in momentum, $u = \sqrt{\gamma^2 - 1}$.

For $dn/dx = Kx^{-p}$, integration gives, for $x_{min} < x_{dn}$,

$$\xi_e^{(x)} = \left(\frac{x_{min}}{x_{dn}}\right)^{p-1}, \qquad \epsilon_e^{(x)} = \left(\frac{x_{min}}{x_{dn}}\right)^{p-2}, \tag{A10}$$

where $x_{min} = \sqrt{1 + u_{min}^2} - 1$. For Newtonian shocks with shock velocity $\beta \ll 1$, for a power law in x, we have $x_{min} \approx \frac{1}{2}u_{min}^2 = \frac{1}{2}\beta_{min}^2 = \frac{p-2}{p-1}\frac{m_p}{m_e}\frac{\epsilon_{e,pl}}{\xi_{e,pl}}\frac{1}{2}\beta^2$. Thus, for $u_{min} \ll 1$,

$$\xi_e^{(x)} \propto u_{min}^{2(p-1)}, \qquad \epsilon_e^{(x)} \propto u_{min}^{2(p-2)}. \tag{A11}$$

For the momentum-space distribution $dn/du = Ku^{-p}$, the number fraction is

$$\xi_e^{(u)} = u_{min}^{p-1} \propto \beta^2, \text{ for } 3 < p < 2, \tag{A12}$$

while

$$\epsilon_e^{(u)} = \frac{\int_1^\infty u^{-p}(\sqrt{1+u^2} - 1)\,du}{\int_{u_{min}}^\infty u^{-p}(\sqrt{1+u^2} - 1)\,du}. \tag{A13}$$

Since the low-u integrand scales as u^{2-p},

$$\epsilon_e^{(u)} = C_p \text{ for } 3 < p < 2, \tag{A14}$$

where C_p is p dependent constant. Thus, ξ_e remains dependent on u_{min} in both parameterizations, while ϵ_e becomes insensitive to x_{min} for $2 < p < 3$ in the momentum-space formulation. In this work, we adopt $dn/du \propto u^{-p}$, for which ϵ_e provides a robust measure of the energy carried by the nonthermal particles. Figure A2 illustrates these different cutoff dependences and highlights the robustness of ϵ_e in the momentum-space parameterization.

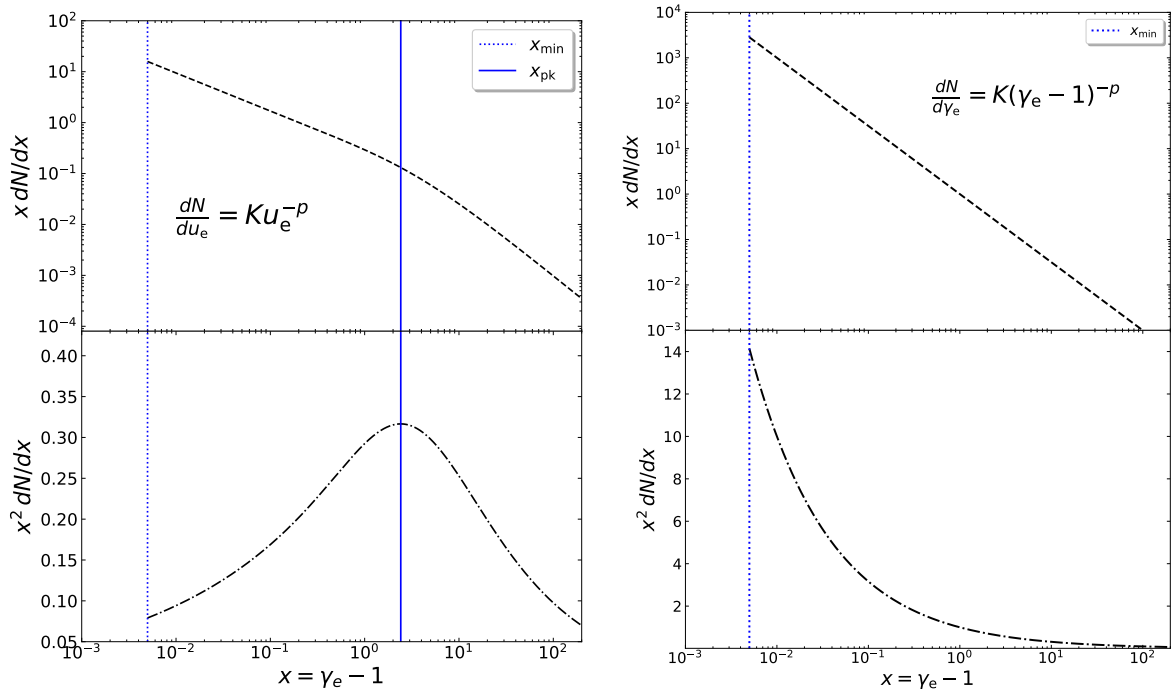


Figure A1. Illustration of the DN regime from shock microphysics. The lower and upper bounds on both panels are$(u_{\rm e,min}, u_{\rm e,max}) = (10^{-1}, 10^{7})$ with power-law index $p = 2.5$. Both right and left plots show particle number (upper panel; dashed black curve) and energy (lower panel; dotted–dashed curve) distributions as functions of the normalized kinetic energy $x \equiv \gamma_{\rm e} - 1$. Vertical dotted lines in both panels indicate $x_{\rm min} = \frac{1}{2}u_{\rm e,min}^2$. Left: the number density and kinetic energy distribution for a power-law distribution of nonthermal particles, $dN/du_{\rm e}$, as a function of the normalized proper speed $u_{\rm e}$. The solid vertical lines indicate $x_{\rm pk}$ (Equation A8), the location of the most energetic particles in the distribution. Right: shows the number density and kinetic energy distribution for a power-law distribution of nonthermal particles, $dN/d\gamma_{\rm e}$, as a function of the normalized proper speed $\gamma_{\rm e} - 1$.

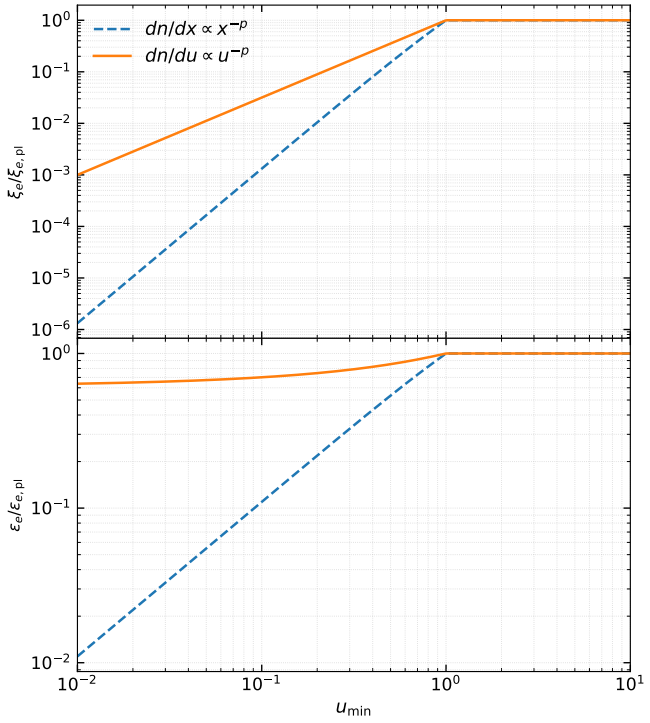


Figure A2. Illustration of ξ_e and $\epsilon_{\rm e}$ as a function of $u_{\rm min}$ for $p = 2.5$. Here, $\xi_{\rm e,pl}$ and $\epsilon_{\rm e,pl}$ correspond to number and energy fraction in the full power-law distribution. The top and middle panels show the accelerated-particle number fraction $\xi_{\rm e}$ and kinetic-energy fraction $\epsilon_{\rm e}$, respectively. Dashed blue and solid orange curves correspond to power-law distributions in kinetic energy, $dn/dx \propto x^{-p}$, and momentum, $dn/du \propto u^{-p}$, respectively.

Appendix B
Onset of the Radiative Phase for a Spherical Blast Wave

We consider a spherical blast wave of energy E propagating into a uniform ambient medium of number density n. Post-deceleration, the evolution is well described by the adiabatic Sedov–Taylor solution (L. I. Sedov 1959; G. I. Taylor 1950), until radiative losses become important. The cooling function is given by $\Lambda_{\rm net} = \Lambda_{\rm N} n_{\rm i} n_{\rm e}$ (where $n_{\rm i}$ and $n_{\rm e}$ are the number densities of ions and electrons, respectively). For a gas with internal energy U, the cooling timescale is given as $t_{\rm cool} = U/\Lambda_{\rm net}$. The transition to the radiative phase is defined by the condition that the post-shock cooling time becomes comparable to the dynamical time (D. F. Cioffi et al. 1988; B. T. Draine 2011). Following B. T. Draine (2011), the post-shock temperature is $T = \frac{3}{16}\frac{\mu m_p}{k_B} v_s^2$ (where $v_{\rm s}$ is the shock velocity). This gives

$$t_{\rm cool} = \frac{9}{16}\frac{\mu m_p}{n\Lambda(T)} v_s^2. \tag{B1}$$

In the temperature range $T \sim 10^5$–10^6K, the cooling function may be approximated as (R. S. Sutherland & M. A. Dopita 1993)

$$\Lambda_{\rm N}(T) \approx 2 \times 10^{-22}\left(\frac{T}{10^6\ \ {\rm K}}\right)^{-0.7} \quad {\rm erg\ cm^3\ s^{-1}}, \tag{B2}$$

which when substituted in Equation (B1) gives

$$t_{\rm cool} \approx 1.1 \times 10^4 \quad n_0^{-1}\left(\frac{v_s}{200 \quad {\rm km\ s^{-1}}}\right)^{3.4} \quad {\rm yr}. \tag{B3}$$

Equating $t_{\rm cool} \sim t$, one obtains a characteristic transition velocity

$$v_{\rm rad} \approx 200 \quad E_{51}^{1/15} n_0^{2/15} \quad {\rm km\ s^{-1}}, \tag{B4}$$

in agreement with detailed radiative blast-wave calculations (D. F. Cioffi et al. 1988). The preceding evolution follows the Sedov–Taylor solution (L. I. Sedov 1959; G. I. Taylor 1950),

$$\begin{aligned} v_s(t) &= 523 \quad E_{51}^{1/5} n_0^{-1/5} t_{10{\rm kyr}}^{-3/5} \quad {\rm km\ s^{-1}}, \\ R(t) &= 13.4 \quad E_{51}^{1/5} n_0^{-1/5} t_{10{\rm kyr}}^{2/5} \quad {\rm pc}, \end{aligned} \tag{B5}$$

where $t_1 0{\rm kyr} = t/10$ kyr. Setting $v_s = v_{\rm rad}$, the transition time is

$$t_{\rm rad} \approx 5 \times 10^4 \quad E_{51}^{4/17} n_0^{-9/17} \quad {\rm yr}, \tag{B6}$$

and the corresponding radius is

$$R_{\rm rad} \approx 25.4 \quad E_{51}^{5/17} n_0^{-7/17} \quad {\rm pc}. \tag{B7}$$

For a canonical explosion with $E_{51} = 1$, the transition properties for representative ambient densities are

$$\begin{aligned} &n = 1 \quad {\rm cm^{-3}}: t_{\rm rad} \approx 5 \times 10^4 \quad {\rm yr}, \\ &\quad R_{\rm rad} \approx 25.4 \quad {\rm pc}, \\ &\quad n = 0.1 \quad {\rm cm^{-3}}: \quad t_{\rm rad} \approx 1.8 \times 10^5 \quad {\rm yr}, \\ &\quad R_{\rm rad} \approx 67.1 \quad {\rm pc}, \\ &\quad n = 0.01 \quad {\rm cm^{-3}}: \quad t_{\rm rad} \approx 6.4 \times 10^5 \quad {\rm yr}, \\ &\quad R_{\rm rad} \approx 177 \quad {\rm pc}. \end{aligned} \tag{B8}$$

These results show that, while the transition velocity is nearly universal, the corresponding time and radius depend sensitively on the ambient density, increasing substantially in environments of lower density (B. T. Draine 2011).

Appendix C
Normalization Factors in Blast-wave Dynamics

Equation (10) captures the correct dynamical scaling but neglects order-unity normalization factors associated with the detailed structure of the self-similar blast wave. Here, we summarize the exact corrections in the two asymptotic regimes.

C.1. Ultrarelativistic Regime

For $u \gg 1$, the shock evolution is described by the Blandford–McKee (R. D. Blandford & C. F. McKee 1976; hereafter BM76) self-similar solution. In this regime, the normalized proper speed approaches the Lorentz factor of the shock front,

$$u \simeq \Gamma. \tag{C1}$$

The BM76 solution gives

$$E = \frac{8\pi}{17 - 4k} \rho_1 \Gamma^2 R^3 c^2, \tag{C2}$$

where the external density profile is assumed to be

$$\rho_1(R) \propto R^{-k}. \tag{C3}$$

The swept-up mass is

$$M(<R) = \int_0^R 4\pi r^2 \rho_1(r) dr = \frac{4\pi}{3 - k} \rho_1 R^3. \tag{C4}$$

Combining these expressions gives

$$u^2 = \frac{17 - 4k}{2(3 - k)} \frac{E}{M(<R)c^2}. \tag{C5}$$

Therefore, the correction factor in the normalized proper speed relative to the simple estimate is

$$C_u^{\rm BM} = \left[\frac{17 - 4k}{2(3 - k)}\right]^{1/2} = \begin{cases} 1.68, & k = 0, \\ 1.80, & k = 1, \\ 2.12, & k = 2. \end{cases} \tag{C6}$$

Since the shock radius satisfies $R \simeq ct$ in the ultrarelativistic limit, the same factors correspond approximately to the normalization correction in $R(t)$ at a fixed lab-frame time.

C.2. Newtonian Regime

At late times, when $u \ll 1$, the blast wave approaches the Sedov–Taylor solution. The shock velocity can be written as (O. Petruk 2000)

$$v^2 = \frac{16\pi}{(5 - k)^2 (3 - k) \alpha_A} \frac{E}{M(<R)}, \tag{C7}$$

where for α_A we use the approximation of J. P. Ostriker & C. F. McKee (1988) for a spherical blast wave (Equation (44) of O. Petruk 2000),

$$\alpha_A = \frac{16\pi}{3(5 - k)^2} \cdot \frac{11\hat{\gamma} - 5 - k(\hat{\gamma} - 1)}{(\hat{\gamma}^2 - 1)[5\hat{\gamma} + 1 - k(\hat{\gamma} + 1)]}. \tag{C8}$$

Taking $\hat{\gamma} = 5/3$ as the adiabatic index of a nonrelativistic gas, we obtain the correction factor in the normalized proper speed,

$$C_u^{\rm ST} = \left[\frac{16\pi}{(5 - k)^2 (3 - k) \alpha_A}\right]^{1/2} = \begin{cases} 1.116, & k = 0, \\ 1.29, & k = 1, \\ 1.63, & k = 2. \end{cases} \tag{C9}$$

The correction to the shock radius is smaller because the Sedov–Taylor solution gives

$$R \propto t^{2/(5-k)}. \tag{C10}$$

Therefore, the radius correction is

$$C_R = (C_u^{\rm ST})^{2/(5-k)}, \tag{C11}$$

yielding

$$C_R = \begin{cases} 1.045, & k = 0, \\ 1.136, & k = 1, \\ 1.387, & k = 2. \end{cases} \tag{C12}$$

Thus, the exact self-similar solutions modify the approximate blast-wave normalization by factors of order unity. For the radius at a fixed lab-frame time, the corresponding correction factors are approximately

$$C_R \simeq \begin{cases} 1.68,\ 1.80,\ 2.12, & u \gg 1, \\ 1.76,\ 1.83,\ 2.00, & u \ll 1, \end{cases} \tag{C13}$$

for $k = 0$, 1, 2, respectively. These corrections modify the normalization of the blast-wave solution but do not change its fundamental scaling.

Appendix D
Useful Expressions in the DN Regime

In this appendix, we give useful expressions for typical dynamical and spectral quantities. As in the main text, we use a value of $\gamma_{\rm dn} = \sqrt{2}$ and $p = 2.5$ throughout.

The deceleration radius $R_{\rm dec}$ is given by (for $u_0 \gg 1$) as

$$R_{\rm dec} = \left[\frac{(3-k)E}{4\pi u_0^2 A c^2}\right]^{\frac{1}{(3-k)}} \approx \begin{cases} 1.2\times 10^{17} u_2^{-\frac{2}{3}} E_{\rm iso,53}^{\frac{1}{3}} n_0^{-\frac{1}{3}}\,{\rm cm}(k=0), \\ 1.8\times 10^{15} u_2^{-2} E_{\rm iso,53} A_\star^{-1}\,{\rm cm}(k=2), \end{cases} \tag{D1}$$

where we use the typical Lorentz factor and isotropic kinetic energy of outflow for GRB afterglows. Here, $u_2 = u/10^2$, $E_{\rm iso,53} = E_{\rm iso}/10^{53}{\rm erg}$, $n_0 = n/1cm^{-3}$, and $A_\star = A/5\times 10^{11}{\rm gm\ cm^{-1}}$ (R. A. Chevalier & Z.-Y. Li 1999). The observed deceleration time for $u_0 \gg 1$ with $E_{\rm iso}$ can be written as

$$t_{\rm dec} \approx \frac{R_{\rm dec}}{2u_0^2 c} \approx \begin{cases} 194.4 u_2^{-\frac{8}{3}} E_{\rm iso,53}^{\frac{1}{3}} n_0^{-\frac{1}{3}}\,{\rm sec}(k=0), \\ 2.9 u_2^{-4} E_{\rm iso,53} A_\star^{-1}\,{\rm sec}(k=2). \end{cases} \tag{D2}$$

The Newtonian transition radius can be expressed as (for $u_0 > u_{\rm n} = 1$)

$$R_{\rm N} = \left[\frac{(3-k)E}{4\pi A u_{\rm N}^2 c^2}\right]^{\frac{1}{(3-k)}} \approx \begin{cases} 0.2 E_{51}^{\frac{1}{3}} n_0^{-\frac{1}{3}}\,{\rm pc}(k=0), \\ 0.06 E_{51} A_\star^{-1}\,{\rm pc}(k=2). \end{cases} \tag{D3}$$

The DN transition radius is (for $u_0 > u_{\rm DN}$)

$$R_{\rm DN} = \left[\frac{(3-k)E}{4\pi A u_{\rm DN}^2 c^2}\right]^{\frac{1}{(3-k)}} \approx \begin{cases} 0.53 n_0^{-\frac{1}{3}} E_{51}^{\frac{1}{3}} \tilde{f}(p)^{\frac{1}{3}} \xi_{e0}^{-\frac{1}{3}} \epsilon_{e,-1}^{\frac{1}{3}}\,{\rm pc}(k=0), \\ 1.62 A_\star^{-1} E_{51} \tilde{f}(p) \xi_{e0}^{-1} \epsilon_{e,-1}\,{\rm pc}(k=2). \end{cases} \tag{D4}$$

The cyclotron frequency in the DN regime is given as (for $t > t_{\rm DN}$)

$$\nu_{\rm B} \equiv \frac{q_e B}{2\pi m_e c} = \frac{q_e}{2\pi m_e c}\sqrt{16\pi\epsilon_{\rm B} A R_{\rm DN}^{-k} u_{\rm DN}^2 c^2}\left(\frac{t}{t_{\rm DN}}\right)^{-\frac{3}{5-k}} \approx \begin{cases} 14.5 n_0^{\frac{1}{2}} \tilde{f}(p)^{-\frac{1}{2}} \xi_{e0}^{\frac{1}{2}} \epsilon_{e,-1}^{-\frac{1}{2}} \epsilon_{B,-2}^{\frac{1}{2}} \left(\frac{t}{t_{\rm DN}}\right)^{-\frac{3}{5}} {\rm kHz}(k=0,\ p=2.5), \\ 1.6 E_{51}^{-1} A_\star^{\frac{1}{2}} \tilde{f}(p)^{-\frac{3}{2}} \xi_{e0}^{\frac{3}{2}} \epsilon_{e,-1}^{-\frac{3}{2}} \epsilon_{B,-2}^{\frac{1}{2}} \left(\frac{t}{t_{\rm DN}}\right)^{-1} {\rm kHz}(k=2,\ p=2.5) \end{cases}. \tag{D5}$$

The DN cooling LF $\gamma_{\rm c}$ is given by (for $t > t_{\rm DN}$)

$$\gamma_{\rm c} \equiv \frac{6\pi m_e c}{\sigma_{\rm T} B^2 t} = \frac{3 m_e (u_{\rm DN} E)^{\frac{k-1}{3-k}}}{8\sigma_{\rm T}\epsilon_{\rm B} A}\left(\frac{t}{t_{\rm DN}}\right)^{\frac{k+1}{5-k}} \approx \begin{cases} 2.5\times 10^5 E_{51}^{\frac{1}{3}} n_0^{-1}\left[\frac{G(p)}{G(2.5)}\right]^{\frac{1}{6}} \xi_{e0}^{-\frac{1}{6}} \epsilon_{e,-1}^{\frac{1}{6}} \epsilon_{B,-2}^{-1} \left(\frac{t}{t_{\rm DN}}\right)^{\frac{1}{5}} (k=0), \\ 4.1\times 10^6 E_{51} A_\star^{-1}\left[\frac{G(p)}{G(2.5)}\right]^{-1} \xi_{e0}\, \epsilon_{e,-1}^{-1} \epsilon_{B,-2}^{-1} \left(\frac{t}{t_{\rm DN}}\right) (k=2). \end{cases} \tag{D6}$$

The cooling break $\nu_{\rm c}$ during the DN phase is (for $t > t_{\rm DN}$)

$$h\nu_{\rm c} \equiv h\gamma_{\rm c}^2 \nu_{\rm B} \approx \begin{cases} 3.6 E_{51}^{\frac{2}{3}} n_0^{-1} \tilde{f}(p)^{-\frac{1}{6}} \xi_{e0}^{\frac{1}{6}} \epsilon_{e,-1}^{-\frac{1}{6}} \epsilon_{B,-2}^{-\frac{3}{2}} \left(\frac{t}{t_{\rm DN}}\right)^{-\frac{1}{5}} {\rm eV}(k=0,\ p=2.5), \\ 108.9 E_{51}^{\frac{3}{2}} A_\star^{-\frac{3}{2}} \tilde{f}(p)^{-\frac{7}{2}} \xi_{e0}^{\frac{7}{2}} \epsilon_{e,-1}^{-\frac{7}{2}} \epsilon_{B,-2}^{\frac{3}{2}} \left(\frac{t}{t_{\rm DN}}\right) {\rm eV}(k=2,\ p=2.5), \end{cases} \tag{D7}$$

which shows that, in the DN regime for a constant-density medium ($k = 0$), the cooling break is just below the optical band, while for a wind-like medium ($k = 2$), it lies in the ultraviolet band. The minimal frequency $\nu_{\rm m}$ in the DN regime is (for $t > t_{\rm DN}$)

$$\nu_{\rm m} \equiv \gamma_{\rm dn}^2 \nu_{\rm B} \approx \begin{cases} 28.9 n_0^{\frac{1}{2}} \tilde{f}(p)^{-\frac{1}{2}} \xi_{e0}^{\frac{1}{2}} \epsilon_{e,-1}^{-\frac{1}{2}} \epsilon_{B,-2}^{\frac{1}{2}} \left(\frac{t}{t_{\rm DN}}\right)^{-\frac{3}{5}} {\rm kHz}(k=0,\ p=2.5), \\ 3.2 E_{51}^{-1} A_\star^{\frac{1}{2}} \tilde{f}(p)^{-\frac{3}{2}} \xi_{e0}^{\frac{3}{2}} \epsilon_{e,-1}^{-\frac{3}{2}} \epsilon_{B,-2}^{\frac{1}{2}} \left(\frac{t}{t_{\rm DN}}\right)^{-1} {\rm kHz}(k=2,\ p=2.5). \end{cases} \tag{D8}$$

The maximum spectral luminosity in the DN phase is (for $t > t_{\rm DN}$)

$$L_{\nu,\max} \equiv N_{\rm rel}\frac{m_e c^2}{3q_e}\sigma_{\rm T} B \approx \begin{cases} 3.7\times 10^{31} E_{51} n_0^{\frac{1}{2}} \xi_{e0}^{-\frac{2}{3}} \epsilon_{e,-1}^{\frac{1}{3}} \epsilon_{B,-2}^{\frac{1}{2}} \left(\frac{t}{t_{\rm DN}}\right)^{-\frac{3}{5}} {\rm Hz^{-1}erg\ s}\,(k=0), \\ 4.0\times 10^{30} A_\star^{\frac{3}{2}} \xi_{e0}^{-1} \epsilon_{B,-2}^{\frac{1}{2}} \left(\frac{t}{t_{\rm DN}}\right)^{-1} {\rm Hz^{-1}erg\ s}\,(k=2). \end{cases} \tag{D9}$$

The maximum spectral luminosity $L_{\nu,\max}$ is not the peak spectral luminosity, as the ordering $\nu_{\rm sa} < \nu_{\rm m}$ cannot be obtained for a broad parameter space (see Appendix E).

Appendix E
Implausibility of Realizing the Ordering $\nu_{\rm sa} < \nu_{\rm m}$ in the DN Phase

Assuming that $\nu_{\rm m} < \nu_{\rm sa}$ can be realized in the DN regime, the self-absorption frequency $\nu_{\rm sa}$ can be written as

$$\frac{2k_{\rm B} T \nu_{\rm sa}^2}{c^2} = \frac{L_{\nu,\max}}{4\pi^2 R^2}\left(\frac{\nu_{\rm sa}}{\nu_{\rm m}}\right)^{\frac{1}{3}} \Rightarrow \frac{\nu_{\rm sa}}{\nu_{\rm m}} = \left(\frac{1}{m_e}\frac{L_{\nu,\max}}{8\pi^2 R^2}\frac{1}{\gamma_{\rm dn}^5}\frac{1}{\nu_{\rm B}^2}\right)^{\frac{3}{5}}, \tag{E1}$$

where $k_{\rm B}T \approx \gamma_{\rm dn} m_{\rm e} c^2$ and $\nu_{\rm m} = \gamma_{\rm dn}^2 \nu_{\rm B}$, and $L_{\nu,\max} = N_{\rm rel} P_{\nu,\max} = \xi_{\rm e0} N_{\rm e} \frac{u^2}{u_{\rm DN}^2} \frac{m_{\rm e} c^2}{3 q_{\rm e}} \sigma_{\rm T} B$, where $N_{\rm e}$ is the total number of electrons in the shocked fluid and B is the post-shock magnetic field (such that $\nu_{\rm B} = \frac{q_{\rm e} B}{2\pi m_{\rm e} c}$ is the cyclotron frequency). In the coasting phase,

$$\frac{\nu_{\rm sa}}{\nu_{\rm m}} = \left[\frac{f(p)\epsilon_{\rm e}\sigma_{\rm T} m_{\rm e} c^2}{48\pi^{3/2} q_{\rm e}^3 \sqrt{\epsilon_{\rm B} A}}\right]^{3/5} 2^{\frac{3k-18}{20}} E^{\frac{3(k-2)}{20}} M^{\frac{3(6-k)}{20}} t^{\frac{3(k-4)}{10}} \text{ for } t < t_{\rm dec}$$
$$\approx \begin{cases} 1.6 \times 10^7 \tilde{f}(p)^{\frac{3}{5}} \epsilon_{\rm e,-1}^{\frac{3}{5}} \epsilon_{\rm B,-2}^{-\frac{3}{10}} n_0^{-\frac{9}{10}} E_{51}^{-\frac{3}{10}} M_3^{\frac{9}{10}} t_{100}^{-\frac{6}{5}} \text{ (k=0)} \\ 9.6 \times 10^5 \tilde{f}(p)^{\frac{3}{5}} \epsilon_{\rm e,-1}^{\frac{3}{5}} \epsilon_{\rm B,-2}^{-\frac{3}{10}} A_\star^{-\frac{3}{10}} M_3^{\frac{6}{5}} t_{100}^{-\frac{3}{5}} \text{ (k=2)} \end{cases}, \tag{E2}$$

where $t_{100} = t/100$ days. In the adiabatic phase,

$$\frac{\nu_{\rm sa}}{\nu_{\rm m}} = \left[f(p)\frac{m_{\rm e} c^2 \sigma_{\rm T}}{24 q_{\rm e}^3} \frac{\epsilon_{\rm e}}{\epsilon_{\rm B}^{\frac{1}{2}}}\right]^{\frac{3}{5}} \left(\frac{E}{R}\right)^{\frac{3}{10}}$$
$$\approx 2^{\frac{3}{10(k-3)}} 3^{\frac{3(k-4)}{10(k-3)}} \left(\frac{m_{\rm e}}{m_{\rm p}}\right)^{\frac{3(7-2k)}{10(3-k)}} \times \left(\frac{m_{\rm e}\sigma_{\rm T} c^2}{12 q_{\rm e}^3}\right)^{\frac{3}{5}} f(p)^{\frac{3}{10(k-3)}} \epsilon_{\rm e}^{\frac{3}{10(k-3)}} \epsilon_{\rm B}^{-\frac{3}{10}} \xi_{\rm e0}^{\frac{3(7-2k)}{10(3-k)}} \times (4\pi A c^2)^{\frac{3}{10(3-k)}} E^{\frac{3(2-k)}{10(3-k)}} \left(\frac{u}{u_{\rm dn}}\right)^{\frac{3}{5(3-k)}}$$
$$= \begin{cases} 6.3 \times 10^5 \tilde{f}(p)^{-\frac{1}{10}} \epsilon_{\rm e,-1}^{-\frac{1}{10}} \epsilon_{\rm B,-2}^{-\frac{3}{10}} \xi_{e0}^{\frac{7}{10}} n_0^{\frac{1}{10}} E^{\frac{1}{5}} \left(\frac{u}{u_{\rm dn}}\right)^{\frac{1}{5}} \text{ (k=0)} \\ 2.6 \times 10^5 \tilde{f}(p)^{\frac{3}{5}} \epsilon_{\rm e,-1}^{\frac{3}{5}} \epsilon_{\rm B,-2}^{-\frac{3}{10}} \xi_{e0}^{\frac{9}{10}} A_\star^{\frac{3}{10}} \left(\frac{u}{u_{\rm dn}}\right)^{\frac{3}{5}} \text{ (k=2)} \end{cases}. \tag{E3}$$

Equations E2–E3 show that, for any reasonable choice of microphysical parameters and bulk energetics, $\nu_1/\nu_{\rm m} < 1$ is not realized. This implies that the ordering, $\nu_1/\nu_{\rm m} < 1$, cannot be achieved over a broad region of parameter space in the DN phase. Physically, this is expected since, in this regime, $\nu_{\rm m}$ lies close to the cyclotron frequency. Achieving $\nu_1 < \nu_{\rm m}$ would therefore require the self-absorption frequency to be pushed below the cyclotron frequency, which is difficult to realize in practice.

Appendix F
Useful Tables

In this appendix, we provide a few useful tables. Table F1 summarizes the temporal scalings of the various physical quantities in the adiabatic phase for $u_0 > u_{\rm DN}$, while Table F2 lists their values at the deep Newtonian transition time, $t_{\rm DN}$.

Table F1
Time-dependent Scaling Relations for Key Dynamical and Radiative Quantities in the Newtonian and the DN Regime in a Spherical Blast Wave Expanding into a Stratified External Medium with Density Profile $\rho_{\rm ext} \propto R^{-k}$

Quantity	$t_{\rm N} < t < t_{\rm DN}$	$t > t_{\rm DN}$
u	$u_{\rm DN}\left(\frac{t}{t_{\rm DN}}\right)^{\frac{3-k}{k-5}}$	$u_{\rm DN}\left(\frac{t}{t_{\rm DN}}\right)^{\frac{3-k}{k-5}}$
$\xi_{\rm e}$	ξ_{e0}	$\xi_{e0}\left(\frac{t}{t_{\rm DN}}\right)^{\frac{2(3-k)}{k-5}}$
N_p	$N_{\rm p,DN}\left(\frac{t}{t_{\rm DN}}\right)^{\frac{2(3-k)}{5-k}}$	$N_{\rm p,DN}\left(\frac{t}{t_{\rm DN}}\right)^{\frac{2(3-k)}{5-k}}$
N_e	$N_{\rm e,DN}\left(\frac{t}{t_{\rm DN}}\right)^{\frac{2(3-k)}{5-k}}$	$N_{\rm e,DN}$
$e_{\rm int}$	$e_{\rm int,DN}\left(\frac{t}{t_{\rm DN}}\right)^{-\frac{6}{5-k}}$	$e_{\rm int,DN}\left(\frac{t}{t_{\rm DN}}\right)^{-\frac{6}{5-k}}$
ν_B	$\nu_{\rm B,DN}\left(\frac{t}{t_{\rm DN}}\right)^{-\frac{3}{5-k}}$	$\nu_{\rm B,DN}\left(\frac{t}{t_{\rm DN}}\right)^{-\frac{3}{5-k}}$
γ_m	$\gamma_{\rm dn}\left(\frac{t}{t_{\rm DN}}\right)^{-\frac{2(3-k)}{5-k}}$	$\gamma_{\rm dn}$
γ_c	$\gamma_{\rm c,DN}\left(\frac{t}{t_{\rm DN}}\right)^{\frac{1+k}{5-k}}$	$\gamma_{\rm c,DN}\left(\frac{t}{t_{\rm DN}}\right)^{\frac{1+k}{5-k}}$
ν_m	$\gamma_{\rm dn}^2 \nu_{\rm B,DN}\left(\frac{t}{t_{\rm DN}}\right)^{-\frac{15-4k}{5-k}}$	$\gamma_{\rm dn}^2 \nu_{\rm B,DN}\left(\frac{t}{t_{\rm DN}}\right)^{-\frac{3}{5-k}}$
ν_c	$\gamma_{\rm c,DN}^2 \nu_{\rm B,DN}\left(\frac{t}{t_{\rm DN}}\right)^{\frac{2k-1}{5-k}}$	$\gamma_{\rm c,DN}^2 \nu_{\rm B,DN}\left(\frac{t}{t_{\rm DN}}\right)^{\frac{2k-1}{5-k}}$
$L_{\nu,\max}$	$L_{\nu,\max,\rm DN}\left(\frac{t}{t_{\rm DN}}\right)^{\frac{3-2k}{5-k}}$	$L_{\nu,\max,\rm DN}\left(\frac{t}{t_{\rm DN}}\right)^{-\frac{3}{5-k}}$

Notes. The evolution is presented for two regimes: the Newtonian phase ($t < t_{\rm DN}$) and the deep Newtonian phase ($t > t_{\rm DN}$). Here, u is the proper velocity of the shocked fluid, $\xi_{\rm e}$ is the fraction of accelerated electrons (with pre-deep Newtonian value ξ_{e0}), N_p and N_e are the number of swept-up protons and nonthermal electrons, $e_{\rm int}$ is the internal energy density, and ν_B is the cyclotron frequency. γ_m and γ_c are the minimum and cooling Lorentz factors of the electron distribution, associated with synchrotron frequencies ν_m and ν_c, respectively. $L_{\nu,max}$ is the maximum synchrotron spectral luminosity. All quantities are expressed in terms of their values at the deep Newtonian transition time $t_{\rm DN}$.

Table F2
Key Dynamical and Radiation Quantities Relevant to the Deep Newtonian (DN) Transition of a Nonrelativistic Blast Wave Propagating into an External Medium with Density $\rho_{\rm ext} \propto R^{-k}$

Dynamics	Radiation
$A = m_{\rm p}\, n(R_0)\, R_0^k$	$N_{\rm DN} = \xi_{e0} \cdot \frac{4\pi A R_{\rm DN}^{3-k}}{3-k}$
$R_{\rm nr} = \left[\frac{(3-k)E}{4\pi A c^2}\right]^{\frac{1}{3-k}}$	$e_{\rm int,DN} = 4Ac^2 u_{\rm DN}^2 R_{\rm DN}^{-k}$
$R_{\rm DN} = R_{\rm nr}\left[\frac{1}{\gamma_{\rm dn}} \cdot \frac{(p-2)}{2(p-1)} \cdot \frac{m_{\rm p}}{m_{\rm e}} \cdot \frac{\epsilon_{\rm e}}{\xi_{e0}}\right]^{\frac{1}{3-k}}$	$\nu_{\rm B,DN} = \frac{q_{\rm e}}{2\pi m_{\rm e} c}\sqrt{8\pi\epsilon_{\rm B} e_{\rm int,DN}}$
$u_{\rm DN} = \sqrt{2\gamma_{\rm dn}}\left[\frac{m_{\rm p}}{m_{\rm e}} \cdot \frac{(p-2)}{(p-1)} \cdot \frac{\epsilon_{\rm e}}{\xi_{e0}}\right]^{-\frac{1}{2}}$	$t_{\rm c1,DN} = \frac{3 m_{\rm e} c}{4\epsilon_{\rm B} e_{\rm int,DN}}$
$t_{\rm DN} = \frac{R_{\rm DN}}{u_{\rm DN} c}$	$\gamma_{\rm c,DN} = \frac{t_{\rm c1,DN}}{t_{\rm DN}}$
	$L_{\nu,\rm max,DN} = N_{\rm e,DN} \cdot \frac{m_{\rm e} c^2}{3 q_{\rm e}} \cdot \sigma_{\rm T} \cdot \sqrt{8\pi\epsilon_{\rm B} e_{\rm int,DN}}$

Note. The DN transition occurs at radius $R_{\rm DN}$ and time $t_{\rm DN}$. The parameter ξ_{e0} denotes the fraction of electrons accelerated to relativistic energies at the transition. Quantities are expressed in terms of the total isotropic-equivalent energy E, microphysical parameters $\epsilon_{\rm e}$, $\epsilon_{\rm B}$, power-law index p of the electron distribution, and ambient density normalization $A = m_{\rm p} n(R_0) R_0^k$ at a fiducial radius R_0.

Appendix G
Relating the Observed Time and Emission Radius

The differential relation between the lab-frame time and radius is given by $dt_{\rm lab} = \frac{dR}{\beta c}$, implying $t_{\rm lab}(R) = \int_0^R \frac{dr}{\beta(r)c}$. For our simple spherical dynamics, $u = \tilde{R}^{(k-3)/2}$, where $\tilde{R} = R/R_N$ is the radius normalized by the Newtonian transition radius R_N. Similarly defining a normalized time $\tilde{t} = \frac{ct}{R_N}$, we have $d\tilde{t}_{\rm lab} = \frac{d\tilde{R}}{\beta c}$, where $\beta(\tilde{R}) = (1 + \tilde{R}^{3-k})^{-1/2}$, leading to

$$\tilde{t}_{\rm lab}(\tilde{R}) = \int_0^{\tilde{R}} dx\sqrt{1 + x^{3-k}} = \tilde{R} \times {}_2F_1\left(-\frac{1}{2}, \frac{1}{3-k}, \frac{4-k}{3-k}, -\tilde{R}^{3-k}\right), \quad \text{(G1)}$$

where ${}_2F_1$ is the hypergeometric function. For $k = 2$, it reduces to a simple expression: $\tilde{t}_{\rm lab}(\tilde{R};\, k{=}2) = \frac{2}{3}[(1 + \tilde{R})^{3/2} - 1]$.

The observed time is given by $t(R, \mu) = t_{\rm lab}(R) - \frac{R\mu}{c}$, where $\mu = \cos\theta$ and θ is the angle from our line of sight. Along our line of sight ($\mu = 1$), it reduces to the so-called radial time, $t_r = t_{\rm lab} - \frac{R}{c}$, which in our case is given by

$$\tilde{t}_r(\tilde{R}) = \tilde{R}\left[{}_2F_1\left(-\frac{1}{2}, \frac{1}{3-k}, \frac{4-k}{3-k}, -\tilde{R}^{3-k}\right) - 1\right]. \quad \text{(G2)}$$

However, at a given observed time t, the emission does not arrive only from the line of sight, but from all of the equal arrival time surface (EATS), corresponding to a range of radii. Therefore, one would like to choose a representative radius along the EATS. For example, in the relativistic regime, $\theta = 1/\Gamma$ is chosen (e.g., R. Sari et al. 1998). More generally, this corresponds to the widest point of the EATS, R_*, that corresponds to the outer edge of the image, where $\mu_* = \beta_*$ (J. Granot & R. Sari 2002; J. Granot et al. 2005), where the values of quantities at this point are denoted by an asterisk subscript. Adopting this representative point on the EATS

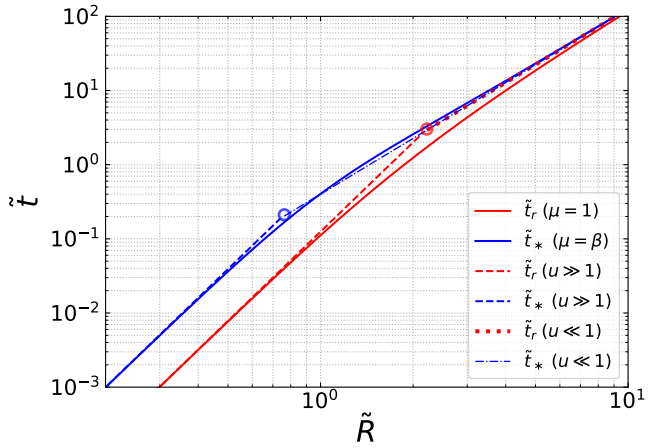


Figure G1. Illustration of the observed normalized time $\tilde{t}$ as a function of the normalized radius $\tilde{R}$ for a spherical blast wave expanding into a constant-density medium ($k = 0$). The blue and red solid curves correspond to the radial normalized time $\tilde{t}_r$ (for $\mu = 1$) and the angular normalized time $\tilde{t}_*$ (for $\mu = \beta$), respectively. The dashed blue and red curves show the ultrarelativistic ($u \gg 1$) asymptotic limits for $\tilde{t}_*$ and $\tilde{t}_r$, respectively. The dotted–dashed blue and dotted red curves represent the Newtonian ($u \ll 1$) asymptotic limits for $\tilde{t}_*$ and $\tilde{t}_r$, which coincide, indicating that line-of-sight effects become negligible in the Newtonian regime. The intersection points of the ultrarelativistic and Newtonian asymptotes are indicated by open circles (red for $\tilde{t}_r$ and blue for $\tilde{t}_*$) (see text for details).

leads to

$$\tilde{t}_*(\tilde{R}) = \tilde{R}\left[{}_2F_1\left(-\frac{1}{2}, \frac{1}{3-k}, \frac{4-k}{3-k}, -\tilde{R}^{3-k}\right) - (1 + \tilde{R}^{3-k})^{-1/2}\right]. \quad \text{(G3)}$$

Figure G1 shows $\tilde{t}_r$ and $\tilde{t}_*$ versus $\tilde{R}$, along with their asymptotic limits. For $\tilde{t} \ll 1$ ($u \gg 1$), we have $\tilde{t}_r \approx \frac{1}{8-2k}\tilde{R}^{4-k}$ and $\tilde{t}_* \approx \frac{5-k}{8-2k}\tilde{R}^{4-k}$, while for $\tilde{t} \gg 1$ ($u \ll 1$), we have $\tilde{t}_r \approx \tilde{t}_* \approx \frac{2}{5-k}\tilde{R}^{(5-k)/2}$. The more realistic $\tilde{t}_*$ (solid blue line) nicely agrees with our approximations (dashed and dashed–dotted blue lines), where we primarily use the $u \ll 1$ approximation ($\tilde{t}_r \approx \tilde{t}_* \approx \frac{2}{5-k}\tilde{R}^{(5-k)/2}$) for $t \geqslant t_N \Leftrightarrow \tilde{t} \geqslant \frac{2}{5-k}$ ($u \leqslant 1 \Leftrightarrow \tilde{R} \geqslant 1$).

Appendix H
Derivation of DN Scalings in the Adiabatic Phase

In this appendix, we consider the DN phase scalings in the adiabatic phase. We consider the adiabatic expansion of a spherical blast wave post-deceleration in a cold and stratified medium described by profile AR^{-k}. As the flow speed drops below the critical proper $u < u_{\rm DN}$, the minimal LF of the relativistic electrons saturates to the value $\gamma_{\rm dn}$. Let relativistic electrons be a fraction $\xi_{\rm e}$ that carry a fraction $\epsilon_{\rm e}$ of the internal energy density, while the post-shock magnetic field carries $\epsilon_{\rm B}$ of the internal energy density. The adiabatic evolution of the blast wave for $R > R_{\rm dec}$ is given as

$$M(<R)c^2u^2 = C_{\rm u}^2 E \ \text{ for } R \geqslant R_{\rm dec} \tag{H1}$$

where E is the total energy in the outflow. Here we assume the normalization $C_{\rm u}$ to be unity for convenience (for exact numerical value see Appendix C).

The minimal LF $\gamma_{\rm m}$ is given as

$$\frac{\gamma_{\rm m}}{G(p)} - 1 \approx \frac{\epsilon_{\rm e}}{\xi_{\rm e}}\frac{m_{\rm p}}{m_{\rm e}}\frac{u^2}{2} \text{ for } u \ll 1 \tag{H2}$$

where $G(p) = \frac{(p-2)}{(p-1)}$, and p is the power-law index of the relativistic electrons.

The critical proper speed $u_{\rm DN}$ can be estimated as

$$u_{\rm DN}^2 = \frac{2}{f(p)}\frac{m_{\rm e}}{m_{\rm p}}\frac{\xi_{\rm e0}}{\epsilon_{\rm e}}, \tag{H3}$$

which shows that the proper critical speed $u_{\rm DN}$ is not a hydrodynamical transition but is decided by the microphysics of particle acceleration. Here $f(p) \equiv G(p)/(\gamma_{dn} - G(p))$.

The DN radius $R_{\rm DN}$ and the corresponding DN time $t_{\rm DN}$ are

$$\begin{aligned} R_{\rm DN} &\equiv R(u = u_{\rm DN}) = \left(\tfrac{(3-k)E}{4\pi Ac^2}\right)^{\frac{1}{3-k}} u_{\rm DN}^{\frac{2}{k-3}}, \\ t_{\rm DN} &\equiv f_{\rm k}\frac{R_{\rm DN}}{u_{\rm DN}c} = f_{\rm k}\frac{1}{c}\left(\tfrac{(3-k)E}{4\pi Ac^2}\right)^{\frac{1}{3-k}} u_{\rm DN}^{\frac{5-k}{k-3}}. \end{aligned} \tag{H4}$$

where $f_{\rm k} = 2/(5-{\rm k})$ is motivated in Appendix G. For the rest of the analysis we will this factor to be unity as our primary objective is obtain the scalings.

The fraction of power-law electrons in relativistic electrons is given as

$$\xi_{\rm e} = \xi_{e0}\frac{u^2}{u_{\rm DN}^2}. \tag{H5}$$

Relativistic electrons $N_{\rm rel}$: The total number of electrons in the shocked fluid is given as

$$N_{\rm e} = \frac{M(<R)}{m_{\rm p}} = \frac{E}{m_{\rm p}c^2u^2}. \tag{H6}$$

The number of relativistic electrons in the shocked fluid is given as

$$\begin{aligned} N_{\rm rel} &= \xi_{\rm e}N_{\rm e} = \xi_{\rm e0}N_{\rm e}\tfrac{u^2}{u_{\rm DN}^2} \\ &= \tfrac{\xi_{\rm e0}E}{m_{\rm p}u_{\rm DN}^2c^2} = \tfrac{f(p)\epsilon_{\rm e}E}{2m_{\rm e}c^2}, \end{aligned} \tag{H7}$$

which shows that, in the DN regime, the number of relativistic electrons saturates and is equal to the number of relativistic electrons at the appropriate critical speed $u = u_{\rm DN}$. Interestingly, it has no dependence on $\xi_{\rm e,0}$. The proper speed in the deep Newtonian regime can be expressed as

$$\tfrac{u^2}{u_{\rm DN}^2} = \left(\tfrac{R_{\rm DN}}{R}\right)^{3-k} = \left(\tfrac{u_{\rm DN}c}{uc}\tfrac{t_{\rm DN}}{t}\right)^{3-k} < 1 \text{ for } u < u_{\rm DN} \tag{H8}$$

which gives

$$\frac{u}{u_{\rm DN}} = \left(\frac{R}{R_{\rm DN}}\right)^{\frac{k-3}{2}} = \left(\frac{t}{t_{\rm DN}}\right)^{\frac{k-3}{5-k}}. \tag{H9}$$

Cyclotron frequency $\nu_{\rm B}$: The internal energy density $e_{\rm int} = 4\Gamma(\Gamma-1)Ac^2R^{-k}$ is given as

$$\begin{aligned} e_{\rm int} &\approx 2u^2c^2AR^{-k} = e_{\rm int,DN}\left(\frac{R}{R_{\rm DN}}\right)^{-3} \\ &= e_{\rm int,DN}\left(\frac{t}{t_{\rm DN}}\right)^{\frac{6}{k-5}} \end{aligned} \tag{H10}$$

where $e_{\rm int,DN} = 2Au_{\rm DN}^2c^2R_{\rm DN}^{-k} = \frac{(3-k)^{\frac{k}{k-3}}}{2\pi}(4\pi Ac^2)^{\frac{3}{3-k}}E^{\frac{k}{k-3}}u_{\rm DN}^{\frac{6}{3-k}}$. The post-shock magnetic field strength can be written as

$$\begin{aligned} B &= \sqrt{8\pi\epsilon_{\rm B}e_{\rm int}} = \sqrt{8\pi\epsilon_{\rm B}e_{\rm int,DN}}\left(\frac{t}{t_{\rm DN}}\right)^{\frac{3}{k-5}} \\ &= B_{\rm DN}\left(\frac{t}{t_{\rm DN}}\right)^{\frac{3}{k-5}}, \end{aligned} \tag{H11}$$

where $B_{\rm DN} = \sqrt{8\pi\epsilon_{\rm B}e_{\rm int,DN}}$ can be expressed in terms of the base parameters as

$$\begin{aligned} B_{\rm DN} = {} & 2^{\frac{9-2k}{6-2k}}(3-k)^{\frac{k}{2k-6}}f(p)^{\frac{3}{2k-6}}\left(\frac{m_{\rm e}}{m_{\rm p}}\right)^{\frac{3}{6-2k}} \\ & \times \epsilon_{\rm B}^{\frac{1}{2}}\epsilon_{\rm e}^{\frac{3}{2k-6}}\xi_{\rm e0}^{\frac{3}{6-2k}}(4\pi Ac^2)^{\frac{3}{6-2k}}E^{\frac{k}{2k-6}}. \end{aligned} \tag{H12}$$

The cyclotron frequency can be written as

$$\nu_{\rm B} \equiv \frac{q_{\rm e}B}{2\pi m_{\rm e}c} = \nu_{\rm B,DN}\left(\frac{t}{t_{\rm DN}}\right)^{\frac{3}{k-5}}, \tag{H13}$$

where $\nu_{\rm B,DN} = \frac{q_{\rm e}B_{\rm DN}}{2\pi m_{\rm e}c}$ can be expressed in terms of the basic parameters as

$$\begin{aligned} \nu_{\rm B,DN} = {} & \left(\frac{q_{\rm e}}{2\pi m_{\rm e}c}\right)2^{\frac{9-2k}{6-2k}}(3-k)^{\frac{k}{2k-6}}f(p)^{\frac{3}{2k-6}}\left(\frac{m_{\rm e}}{m_{\rm p}}\right)^{\frac{3}{6-2k}} \\ & \epsilon_{\rm B}^{\frac{1}{2}}\epsilon_{\rm e}^{\frac{3}{2k-6}}\xi_{\rm e0}^{\frac{3}{6-2k}}(4\pi Ac^2)^{\frac{3}{6-2k}}E^{\frac{k}{2k-6}}.. \end{aligned} \tag{H14}$$

Maximum spectral luminosity $L_{\nu,\max}$: The maximum spectral luminosity due to relativistic electrons is given by

$$L_{\nu,\max} = N_{\rm rel} P_{\nu,\max} = N_{\rm rel}\left(\frac{m_{\rm e}c^2}{3q_{\rm e}}\sigma_T B\right) = L_{\nu,max,DN}\left(\frac{t}{t_{\rm DN}}\right)^{\frac{3}{k-5}}, \quad \text{(H15)}$$

where

$$L_{\nu,max,DN} = \frac{f(p)\,\epsilon_{\rm e}E}{2m_{\rm e}c^2}\left(\sqrt{8\pi\epsilon_{\rm B}e_{\rm int,DN}}\,\frac{m_{\rm e}c^2}{3q_{\rm e}}\sigma_T\right), \quad \text{(H16)}$$

which can be expressed in terms of the basic parameters as

$$L_{\nu,max,DN} = \frac{\sigma_{\rm T}}{3q_{\rm e}} 2^{\frac{3}{6-2k}}(3-k)^{\frac{k}{2k-6}}\left(\frac{m_e}{m_p}\right)^{\frac{3}{6-2k}} f(p)^{\frac{3-2k}{6-2k}} \times \epsilon_{\rm B}^{\frac{1}{2}}\epsilon_{\rm e}^{\frac{3-2k}{6-2k}}\xi_{\rm e0}^{\frac{3}{6-2k}}(4\pi Ac^2)^{\frac{3}{6-2k}}E^{\frac{3k-6}{2k-6}}. \quad \text{(H17)}$$

The minimal frequency $\nu_{\rm m}$: The minimal frequency is given as

$$\nu_{\rm m} \equiv \gamma_{\rm dn}^2\nu_{\rm B} = \nu_{\rm m,DN}\left(\frac{t}{t_{\rm DN}}\right)^{\frac{3}{k-5}}, \text{ where } \nu_{\rm m,DN} = \gamma_{\rm dn}^2\nu_{\rm B,DN}\ . \quad \text{(H18)}$$

The cooling frequency $\nu_{\rm c}$: The cooling LF is $\gamma_{\rm c} = \frac{6\pi m_{\rm e}c}{\sigma_T B^2 t}$, while the cyclotron frequency can be written as

$$\nu_{\rm c} \equiv \gamma_{\rm c}^2\nu_{\rm B} = \nu_{\rm c,DN}\left(\frac{t}{t_{\rm DN}}\right)^{\frac{1-2k}{k-5}} \quad \text{where } \nu_{\rm c,DN} = \left(\frac{q_{\rm e}}{2\pi m_{\rm e}c}\right)\left(\frac{6\pi m_{\rm e}c}{\sigma_{\rm T}}\right)^2\frac{1}{B_{\rm DN}^3 t_{\rm DN}^2}. \quad \text{(H19)}$$

The self-absorption frequency $\nu_{\rm sa}$: The self-absorption frequency $\nu_{\rm sa}$ in Spectrum 2 ($\nu_{\rm m} < \nu_{\rm sa}$) can be obtained from the relationship

$$\frac{2k_{\rm B}T\nu_{\rm sa}^2}{c^2} \times \frac{\pi R^2}{d^2} = \frac{L_{\nu,\max}}{4\pi d^2}\left(\frac{\nu_{\rm sa}}{\nu_{\rm m}}\right)^{\frac{1-p}{2}}, \quad \text{(H20)}$$

where $k_{\rm B}T = \gamma_{\rm sa}m_{\rm e}c^2 = \sqrt{\frac{\nu_{\rm sa}}{\nu_{\rm B}}}m_{\rm e}c^2$. Here $k_{\rm B}$ is the Boltzmann constant.

The self-absorption frequency in Spectrum 2 can be written as

$$\nu_{\rm sa} = \left[\frac{1}{m_{\rm e}}\frac{L_{\nu,\max}}{8\pi^2R^2}\gamma_{\rm dn}^{p-1}\nu_{\rm B}^{\frac{p}{2}}\right]^{\frac{2}{p+4}} = \nu_{\rm sa,DN}\left(\frac{t}{t_{\rm DN}}\right)^{\frac{3p+14}{(k-5)(p+4)}}, \quad \text{(H21)}$$

where

$$\begin{aligned}\nu_{\rm sa,DN} &= \left[\frac{1}{m_{\rm e}}\frac{L_{\nu,max,DN}}{8\pi^2R_{\rm DN}^2}\gamma_{\rm dn}^{p-1}\nu_{\rm B,DN}^{\frac{p}{2}}\right]^{\frac{2}{p+4}} \\ &= K_{\rm l}A^{\frac{14+3p}{2(3-k)(p+4)}}E^{\frac{4-6k-pk}{2(3-k)(p+4)}}\gamma_{\rm dn}^{\frac{2(p-1)}{(p+4)}} \times f(p)^{\frac{-4k-2-3p}{2(3-k)(p+4)}}\xi_{\rm e0}^{\frac{14+3p}{2(3-k)(p+4)}}\epsilon_{\rm e}^{\frac{-4k-2-3p}{2(3-k)(p+4)}}\epsilon_B^{\frac{p+2}{2(p+4)}} \\ &= \begin{cases} K_{\rm l}(k=0)A^{\frac{14+3p}{6(p+4)}}E^{\frac{2}{3(p+4)}}\gamma_{\rm dn}^{\frac{2(p-1)}{(p+4)}}f(p)^{\frac{-2-3p}{6(p+4)}}\xi_{\rm e0}^{\frac{14+3p}{6(p+4)}}\epsilon_{\rm e}^{\frac{-2-3p}{6(p+4)}}\epsilon_B^{\frac{p+2}{2(p+4)}}(k=0), \\ K_{\rm l}(k=2)A^{\frac{14+3p}{2(p+4)}}E^{-1}\gamma_{\rm dn}^{\frac{2(p-1)}{(p+4)}}f(p)^{\frac{-10-3p}{2(p+4)}}\xi_{\rm e0}^{\frac{14+3p}{2(p+4)}}\epsilon_{\rm e}^{\frac{-10-3p}{2(p+4)}}\epsilon_B^{\frac{p+2}{2(p+4)}}(k=2), \end{cases} \end{aligned} \quad \text{(H22)}$$

where the constant K_1 is

$$K_{\rm l} = \left[\frac{\sigma_T q_{\rm e}^{p/2-1}}{48\pi^2 m_{\rm e}^{1+p/2}}\right]^{\frac{2}{p+4}} \cdot 2^{\frac{9p+54-4k}{2(3-k)(p+4)}} \cdot \pi^{\frac{2kp-3p+14}{2(3-k)(p+4)}} \cdot c^{\frac{kp+14}{(3-k)(p+4)}} \cdot (3-k)^{-\frac{8+k(p+2)}{2(3-k)(p+4)}} \cdot \left(\frac{m_{\rm e}}{m_{\rm p}}\right)^{\frac{3p+14}{2(3-k)(p+4)}}. \quad \text{(H23)}$$

Spectral luminosity $L_{\nu_{\rm sa}}$ at the self-absorption frequency: The spectral luminosity at the self-absorption frequency can be estimated as

$$L_{\nu_{\rm sa}} = L_{\nu_{\rm sa,DN}}\left(\frac{t}{t_{\rm DN}}\right)^{\frac{2p+13}{(k-5)(p+4)}}, \tag{H24}$$

where

$$\begin{aligned} L_{\nu_{\rm sa,DN}} &= L_{\nu,{\rm max},DN}\nu_{\rm sa,DN}^{\frac{1-p}{2}}\nu_{\rm m,DN}^{\frac{p-1}{2}} = K_2 A^{\frac{2p+13}{2(3-k)(p+4)}}E^{\frac{26-13k+4p-2kp}{2(3-k)(p+4)}}\gamma_{\rm dn}^{\frac{5(p-1)}{(p+4)}} \\ &\quad f(p)^{\frac{17-10k-2p}{2(3-k)(p+4)}}\xi_{\rm e0}^{\frac{2p+13}{2(3-k)(p+4)}}\epsilon_{\rm e}^{\frac{17-10k-2p}{2(3-k)(p+4)}}\epsilon_B^{\frac{2p+3}{2(p+4)}} \\ &= \begin{cases} K_2(k=0)A^{\frac{2p+13}{6(p+4)}}E^{\frac{13+2p}{3(p+4)}}\gamma_{\rm dn}^{\frac{5(p-1)}{(p+4)}}f(p)^{\frac{17-2p}{6(p+4)}}\xi_{\rm e0}^{\frac{2p+13}{6(p+4)}}\epsilon_{\rm e}^{\frac{17-2p}{6(p+4)}}\epsilon_B^{\frac{2p+3}{2(p+4)}}(k=0) \\ K_2(k=2)A^{\frac{2p+13}{2(p+4)}}E^{0}\gamma_{\rm dn}^{\frac{5(p-1)}{(p+4)}}f(p)^{-\frac{(3+2p)}{2(p+4)}}\xi_{\rm e0}^{\frac{2p+13}{2(p+4)}}\epsilon_{\rm e}^{\frac{-(3+2p)}{2(p+4)}}\epsilon_B^{\frac{2p+3}{2(p+4)}}(k=2) \end{cases}, \end{aligned} \tag{H25}$$

where the constant K_2 is

$$K_2 = \sigma_T^{\frac{5}{p+4}}q_e^{\frac{2p-7}{p+4}}(3-k)^{\frac{4p-4-2kp-3k}{2(3-k)(p+4)}}(2^{a_2}3^{b_2}\pi^{c_2}c^{2F_c}m_e^{m_2/2}m_p^{p_2/2})^{\frac{1}{2(3-k)(p+4)}}, \tag{H26}$$

where

$$\begin{aligned} a_2 &= 21 + 6k + 24p - 6kp, \\ b_2 &= -30 + 10k, \\ c_2 &= 2p + 13, \\ F_c &= 19 - 2k - 4p + 2kp, \\ m_2 &= 38 - 4k - 8p + 4kp, \\ p_2 &= -4p - 26. \end{aligned}$$

Appendix I
DN Scalings in the Coasting Phase

In this section, we consider a Newtonian outflow of energy E and mass M launched at a single velocity $u_0 < u_{\rm DN}$. In this scenario, the DN regime is realized at launch itself. The coasting speed u_0 is

$$u_0 = \frac{1}{c}\sqrt{\frac{2E}{M}}. \tag{I1}$$

The critical proper speed $u_{\rm DN}$ is

$$u_{\rm DN}^2 = \frac{2}{f(p)}\frac{m_{\rm e}}{m_{\rm p}}\frac{\xi_{\rm e0}}{\epsilon_{\rm e}}. \tag{I2}$$

The radius is related to the coasting velocity as

$$R = u_0 ct. \tag{I3}$$

The number of relativistic electrons is

$$N_{\rm rel} = \xi_{\rm e0}\frac{u_0^2}{u_{\rm DN}^2}\frac{4\pi AR^{3-k}}{(3-k)m_{\rm p}}. \tag{I4}$$

The post-shock magnetic field is

$$B = \sqrt{16\pi\epsilon_{\rm B}u_0^2Ac^2R^{-k}}. \tag{I5}$$

The cyclotron frequency is given as

$$\nu_{\rm B} = \frac{q_{\rm e}}{2\pi m_{\rm e}c}\sqrt{16\pi\epsilon_{\rm B}u_0^2Ac^2R^{-k}}. \tag{I6}$$

The minimal frequency is given as

$$\nu_{\rm m} = \gamma_{\rm dn}^2\nu_{\rm B} = \gamma_{\rm dn}^2\frac{q_{\rm e}}{2\pi m_{\rm e}c}\sqrt{16\pi\epsilon_{\rm B}u_0^2Ac^2R^{-k}}. \tag{I7}$$

The maximum spectral luminosity is given as (($t < t_{\rm dec}$))

$$\begin{aligned} L_{\nu,{\rm max}} &= N_{\rm rel}\frac{m_{\rm e}c^2}{3q_{\rm e}}\sigma_T B = \frac{16\pi^{3/2}\sigma_T}{3q_e(3-k)} \\ &\quad f(p)\,\epsilon_{\rm e}\,\epsilon_{\rm B}^{\frac{1}{2}}A^{3/2}2^{\frac{8-3k}{4}}\left(\frac{E}{M}\right)^{\frac{3(4-k)}{4}}t^{3-\frac{3k}{2}} \\ &= \begin{cases} \frac{64\pi^{3/2}\sigma_T}{9q_e}f(p)\,\epsilon_{\rm e}\,\epsilon_{\rm B}^{\frac{1}{2}}A^{3/2}\left(\frac{E}{M}\right)^3t^3(k=0), \\ \frac{16\sqrt{2}\pi^{3/2}\sigma_T}{3q_e}f(p)\,\epsilon_{\rm e}\,\epsilon_{\rm B}^{\frac{1}{2}}A^{3/2}\left(\frac{E}{M}\right)^{3/2}(k=2). \end{cases} \end{aligned} \tag{I8}$$

The self-absorption frequency $\nu_{\rm sa}$ is given as ($t < t_{\rm dec}$)

$$\nu_{\rm pk} = \nu_{\rm sa} = \left[\frac{1}{m_{\rm e}}\frac{L_{\nu,\rm max}}{8\pi^2 R^2}\gamma_{\rm dn}^{p-1}\nu_{\rm B}^{\frac{p}{2}}\right]^{\frac{2}{p+4}}$$

$$= \left[\frac{\sigma_{\rm T}}{3(3-k)}\cdot\frac{2^{\frac{16-6k+6p-kp}{8}}\pi^{-\frac{1}{2}-\frac{p}{4}}}{m_e^{1+\frac{p}{2}}c^{\frac{p}{2}}q_e^{1-\frac{p}{2}}}\right]^{\frac{2}{p+4}}\gamma_{\rm dn}^{\frac{2(p-1)}{p+4}}f(p)^{\frac{2}{p+4}}A^{\frac{6+p}{2(p+4)}}\epsilon_{\rm e}^{\frac{2}{p+4}}\epsilon_B^{\frac{2+p}{2(p+4)}}\left(\frac{E}{M}\right)^{\frac{16-6k+p(2-k)}{4(p+4)}}t^{\frac{4-6k-kp}{2(p+4)}}$$

$$= \begin{cases} \left[\frac{\sigma_T}{9}\cdot\frac{2^{\frac{16+6p}{8}}\pi^{-\frac{1}{2}-\frac{p}{4}}}{m_e^{1+\frac{p}{2}}c^{\frac{p}{2}}q_e^{1-\frac{p}{2}}}\right]^{\frac{2}{p+4}}\gamma_{\rm dn}^{\frac{2(p-1)}{p+4}}f(p)^{\frac{2}{p+4}}A^{\frac{6+p}{2(p+4)}}\epsilon_{\rm e}^{\frac{2}{p+4}}\epsilon_B^{\frac{2+p}{2(p+4)}}\left(\frac{E}{M}\right)^{\frac{8+p}{2(p+4)}}t^{\frac{2}{p+4}}(k=0), \\ \left[\frac{\sigma_T}{3}\cdot\frac{2^{\frac{1+p}{2}}\pi^{-\frac{1}{2}-\frac{p}{4}}}{m_e^{1+\frac{p}{2}}c^{\frac{p}{2}}q_e^{1-\frac{p}{2}}}\right]^{\frac{2}{p+4}}\gamma_{\rm dn}^{\frac{2(p-1)}{p+4}}f(p)^{\frac{2}{p+4}}A^{\frac{6+p}{2(p+4)}}\epsilon_{\rm e}^{\frac{2}{p+4}}\epsilon_B^{\frac{2+p}{2(p+4)}}\left(\frac{E}{M}\right)^{\frac{1}{p+4}}t^{-1}(k=2). \end{cases} \quad \text{(I9)}$$

The peak/self-absorption spectral luminosity is given as ($t < t_{\rm dec}$)

$$L_{\nu,\rm sa} = L_{\nu,\rm max}\left(\frac{\nu_{\rm sa}}{\nu_{\rm m}}\right)^{\frac{(1-p)}{2}}$$

$$= K(k,p)f(p)^{\frac{5}{p+4}}\gamma_{\rm dn}^{\frac{5(p-1)}{p+4}}A^{\frac{2p+13}{2(p+4)}}\epsilon_{\rm e}^{\frac{5}{p+4}}\epsilon_B^{\frac{2p+3}{2(p+4)}}\left(\frac{E}{M}\right)^{\frac{(4-k)(2p+13)}{4(p+4)}}t^{\frac{4p+26-2kp-13k}{2(p+4)}}$$

$$= \begin{cases} K(0,p)\gamma_{\rm dn}^{\frac{5(p-1)}{p+4}}f(p)^{\frac{5}{p+4}}\epsilon_{\rm e}^{\frac{5}{p+4}}A^{\frac{2p+13}{2(p+4)}}\epsilon_B^{\frac{2p+3}{2(p+4)}}\left(\frac{E}{M}\right)^{\frac{2p+13}{p+4}}t^{\frac{2p+13}{p+4}}(k=0), \\ K(2,p)\gamma_{\rm dn}^{\frac{5(p-1)}{p+4}}f(p)^{\frac{5}{p+4}}\epsilon_{\rm e}^{\frac{5}{p+4}}A^{\frac{2p+13}{2(p+4)}}\epsilon_B^{\frac{2p+3}{2(p+4)}}\left(\frac{E}{M}\right)^{\frac{2p+13}{2(p+4)}}t^{0}(k=2), \end{cases} \quad \text{(I10)}$$

where

$$K(k,p) = 16\,[3(3-k)]^{-\frac{5}{p+4}}\,2^{\alpha(k,p)}\,\pi^{\frac{4p+26}{4(p+4)}}\,m_e^{\frac{1-p}{p+4}}\,c^{\frac{2(1-p)}{p+4}}\,q_e^{\frac{2p-7}{p+4}}\,\sigma_T^{\frac{5}{p+4}} \quad \text{(I11)}$$

$$\alpha(k,p) = \frac{8-3k}{4} - \frac{(1-p)(4+k)}{4(p+4)} \quad \text{(I12)}$$

$$K(0,p) = 16\cdot\,2^{\frac{3p+7}{p+4}}\,3^{-\frac{10}{p+4}}\,\pi^{\frac{2p+13}{2(p+4)}}\,m_e^{\frac{1-p}{p+4}}\,c^{\frac{2(1-p)}{p+4}}\,q_e^{\frac{2p-7}{p+4}}\,\sigma_T^{\frac{5}{p+4}} \quad \text{(I13)}$$

$$K(2,p) = 16\cdot\,2^{\frac{4p+1}{2(p+4)}}\,3^{-\frac{5}{p+4}}\,\pi^{\frac{2p+13}{2(p+4)}}\,m_e^{\frac{1-p}{p+4}}\,c^{\frac{2(1-p)}{p+4}}\,q_e^{\frac{2p-7}{p+4}}\,\sigma_T^{\frac{5}{p+4}}. \quad \text{(I14)}$$

Appendix J
Velocity Stratification in SNR

We consider the density profile for homologously expanding supernova ejecta, commonly parameterized as (R. A. Chevalier 1982; R. A. Chevalier & C. Fransson 1994)

$$\rho(r,t) = A\,r^{-n}t^{\,n-3}, \quad \text{(J1)}$$

where r is radius, t is time, and A is a constant. Homologous expansion implies $r = vt$, where v is the constant velocity of a given mass shell. Substituting $r = vt$ into the density profile gives

$$\rho(v,t) = A\,(vt)^{-n}t^{\,n-3} = A\,v^{-n}t^{-3}. \quad \text{(J2)}$$

Thus, at a fixed time, the density depends on velocity as $\rho(v) \propto v^{-n}$. The mass per unit velocity interval is

$$\frac{dm}{dv} = 4\pi r^2\rho(r,t)\frac{dr}{dv} = 4\pi A\,(v^2t^2)\,(v^{-n}t^{-3})\,t = 4\pi A\,v^{\,2-n}, \quad \text{(J3)}$$

where we used $r = vt$, $\frac{dr}{dv} = t$, and $\rho(v,t) = Av^{-n}t^{-3}$ The kinetic energy per unit velocity is

$$\frac{dE}{dv} \propto v^2\cdot v^{\,2-n} = v^{\,4-n}. \quad \text{(J4)}$$

The cumulative kinetic energy in material with velocity greater than v is

$$E(>v) = \int_{v}^{v_{\max}} \frac{dE}{dv'} dv' \propto \int_{v}^{v_{\max}} v'^{4-n} dv'. \quad \text{(J5)}$$

For $n > 5$, the integral converges and the upper limit $v_{\max}^{5-n} \to 0$, yielding

$$E(>v) \approx \frac{2\pi A}{n-5} v^{-s} \quad \text{where } s = n - 5\,. \quad \text{(J6)}$$

For $n \approx 9$–10, the stratification index $s = (4, 5)$.

Appendix K
$\Sigma - D$ Relation for Resolved Galactic Supernova Remnants with $p > 2$

The spectral luminosity in PLS G of Spectrum 2 (for $\nu_{\rm G} > \nu_{\rm sa}$) can be written as

$$\begin{aligned} L_{\nu,\rm G} &= L_{\nu,\rm sa}\left(\frac{\nu_{\rm G}}{\nu_{\rm sa}}\right)^{\frac{1-p}{2}} \\ &= L_{\nu,\max}\left(\frac{\nu_{\rm sa}}{\nu_{\rm m}}\right)^{\frac{1-p}{2}}\left(\frac{\nu_{\rm G}}{\nu_{\rm sa}}\right)^{\frac{1-p}{2}} \\ &= L_{\nu,\max}\left(\frac{\nu_{\rm G}}{\nu_{\rm m}}\right)^{\frac{1-p}{2}}, \end{aligned} \quad \text{(K1)}$$

which shows that the spectral luminosity in PLS G can be obtained by extrapolation of the maximum spectral luminosity at $\nu_{\rm G}$. Post-deceleration, the proper speed u can be written as

$$u^2 = \frac{(3-k)ER^{k-3}}{4\pi A c^2}, \text{ for } R > R_{\rm dec}\,, \quad \text{(K2)}$$

such that the internal energy density for $R > R_{\rm dec}$ can be obtained as

$$\begin{aligned} e_{\rm int} &= 4\Gamma(\Gamma-1)AR^{-k}c^2 \approx 2u^2c^2AR^{-k} = 2Ac^2R^{-k} \\ &\times\left(\frac{(3-k)E}{4\pi Ac^2}R^{k-3}\right) \\ &= \frac{(3-k)ER^{-3}}{2\pi} = 2\left(1-\frac{k}{3}\right)\left(\frac{E}{\frac{4\pi}{3}R^3}\right), \end{aligned} \quad \text{(K3)}$$

where we used $\Gamma - 1 \approx \frac{u^2}{2} \ll 1$. It can be seen that, in the post-deceleration phase, the internal energy density is weakly dependent on the stratification of the ambient medium k and independent of the normalization constant of the ambient density A. In fact, for a constant-density medium, it is equal to twice the average energy density within a sphere of radius R.

In the DN regime post-deceleration, the maximum spectral luminosity post-deceleration can be written as

$$\begin{aligned} L_{\nu,\max} &= \xi_{\rm e} N_{\rm e} P_{\nu,\max} = \left(\xi_{\rm e0}\frac{u^2}{u_{\rm DN}^2}\right)\left[\frac{4\pi AR^{3-k}}{(3-k)m_{\rm p}}\right] \\ &\times P_{\nu,\max} = \frac{\sigma_{\rm T}}{3q_{\rm e}}\left(\frac{m_{\rm e}}{m_{\rm p}}\right)\left(\frac{\xi_{e0}E}{u_{\rm DN}^2}\right)\sqrt{8\pi\epsilon_{\rm B}e_{\rm int}}\,, \end{aligned} \quad \text{(K4)}$$

Table K1
Supernova Remnants with Spectral Index $\alpha > 0.5$

Name	Σ (10^{-21}W m^{-2}Hz^{-1}sr^{-1})	D (pc)	α	p
G4.5+6.8 (Kepler)	318.00	5.2	0.64	2.28
G21.8−0.6 (Kes 69)	26.00	30.3	0.56	2.12
G27.4+0.4 (Kes 73)	56.40	10.1	0.68	2.36
G33.6+0.1 (Kes 79)	33.10	20.4	0.51	2.02
G46.8−0.3 (HC30)	9.50	33.7	0.54	2.08
G65.1+0.6	0.18	175.6	0.61	2.22
G78.2+2.1 (γ Cygni)	13.40	20.9	0.51	2.02
G93.7−0.2 (CTB 104A)	1.50	34.9	0.65	2.30
G96.0+2.0	0.07	30.3	0.60	2.20
G111.7−2.1 (Cassiopeia A)	16400.00	4.8	0.77	2.54
G116.9+0.2 (CTB 1)	1.04	15.8	0.57	2.14
G120.1+1.4 (Tycho)	132.00	5.8	0.58	2.16
G132.7+1.3 (HB 3)	1.06	51.2	0.60	2.20
G152.4−2.1	0.06	31.1	0.70	2.40
G160.9+2.6 (HB 9)	0.98	30.2	0.64	2.28
G190.9−2.2	0.05	18.8	0.70	2.40
G296.8−0.3 (1156-62)	4.80	46.7	0.60	2.20
G315.4−2.3 (RCW 86)	4.20	28.1	0.60	2.20
G327.4+0.4 (Kes 27)	10.20	29.6	0.60	2.20
G327.6+14.6 (SN 1006)	3.20	14.8	0.70	2.40
G337.0−0.1 (CTB 33)	134.00	4.2	0.60	2.20
G352.7−0.1	12.50	15.1	0.60	2.20

Note. Surface brightness Σ is in units of 10^{-21}W m^{-2}Hz^{-1}sr^{-1}, diameter D is given in pc, and $p = 2\alpha + 1$. The data are compiled from M. Z. Pavlovic et al. (2014) and D. A. Green (2025). The common names of the remnants are given in brackets.

such that the spectral luminosity in PLS G can be obtained as

$$\begin{aligned} L_{\nu,\rm G} &= L_{\nu,\max}\nu_{\rm m}^{\frac{p-1}{2}}\nu_{\rm G}^{\frac{1-p}{2}} \\ &= 2^{\frac{3(p+1)}{4}}\left(\frac{3-k}{2\pi}\right)^{\frac{p+1}{4}}\left(\frac{q_{\rm e}}{2\pi m_{\rm e}c}\right)^{\frac{p-1}{2}} \\ &\times\frac{\gamma_{\rm dn}^{p-1}}{u_{\rm DN}^2}\left(\frac{\sigma_{\rm T}}{3q_{\rm e}}\right)\left(\frac{m_{\rm e}}{m_{\rm p}}\right)(8\pi\epsilon_{\rm B})^{\frac{p+1}{4}}\xi_{\rm e0} \\ &\times E^{\frac{p+5}{4}}\nu_{\rm G}^{\frac{1-p}{2}}D^{-\frac{3(p+1)}{4}}, \end{aligned} \quad \text{(K5)}$$

where $D = 2R$ is the diameter of the source. The surface brightness in PLS G can be written as

$$\begin{aligned} \Sigma_{\rm G} &= \frac{F_{\nu,\rm G}}{\Omega} = \frac{L_{\rm G}}{4\pi d^2}\frac{1}{\Omega} = \frac{L_{\rm G}}{4\pi d^2}\frac{1}{\frac{\pi R^2}{d^2}} \\ &= \frac{L_{\rm G}}{\pi^2 D^2} = \mathcal{K}\epsilon_{\rm e}\epsilon_{\rm B}^{\frac{p+1}{4}}E^{\frac{p+5}{4}}D^{-\frac{(3p+11)}{4}} \quad \text{for } D > 2R_{\rm dec} \end{aligned} \quad \text{(K6)}$$

where the numerical constant $\mathcal{K}$ is given as (for $p > 2$)

$$\begin{aligned} \mathcal{K} &= \left(\frac{\sigma_{\rm T}}{3q_{\rm e}}\right)\left(\frac{q_{\rm e}}{2\pi m_{\rm e}c}\right)^{\frac{p-1}{2}}f(p)(8\pi)^{\frac{p+1}{4}} \\ &\times\frac{2^{\frac{3p-1}{4}}}{\pi^2}\left(\frac{3-k}{2\pi}\right)^{\frac{p+1}{4}}\gamma_{\rm dn}^{p-1}\nu_{\rm G}^{\frac{1-p}{2}}. \end{aligned} \quad \text{(K7)}$$

Thus, the surface brightness of SNR scales as $\Sigma_{\rm G} \propto D^{-\frac{3p+11}{4}}$, and the normalization $\mathcal{K}$ depends weakly on the stratification index k. Table K1 summarizes the typical diameters, surface brightnesses, and spectral indices (α) of selected Galactic

supernova remnants in the power-law segment (PLS G). The electron energy distribution power-law index is inferred from the spectral index using $p = 2\alpha + 1$, and the table includes only sources with $p > 2$.

K.1. Correction Factors from Exact Self-similar Solutions

The exact Blandford–McKee and Sedov–Taylor self-similar solutions introduce order-unity corrections to the fiducial post-deceleration blast-wave evolution. Following O. Petruk (2000), we write

$$u^2 = C_u^2 u_0^2,\ R = C_R R_0,\ D = C_R D_0, \tag{K8}$$

where

$$C_u = C_u^{\rm ST} = \left[\frac{16\pi}{(5-k)^2(3-k)\alpha_A}\right]^{1/2}, \qquad C_R = C_u^{2/(5-k)}. \tag{K9}$$

Using Equation (C8) for α_A and for $\gamma = 5/3$, $C_u^{\rm ST} \simeq 1.116, 1.29, 1.63$ for $k = 0, 1, 2$, respectively. The corrected proper speed can be written in terms of the physical radius as

$$u^2 = C_u^2 \frac{(3-k)ER^{k-3}}{4\pi Ac^2}, \qquad R > R_{\rm dec}, \tag{K10}$$

such that

$$e_{\rm int} \simeq 2u^2c^2AR^{-k} = C_u^2\frac{(3-k)ER^{-3}}{2\pi}. \tag{K11}$$

In the DN regime, $\xi_{\rm e} \propto u^2$, $N_{\rm e} \propto R^{3-k}$, and $P_{\nu,\max} \propto \sqrt{e_{\rm int}}$, giving

$$L_{\nu,\max} \propto \left(C_u^2 R^{k-3}\right)(R^{3-k})(C_u R^{-3/2}) = C_u^3 R^{-3/2}. \tag{K12}$$

Similarly, since $\nu_{\rm m} \propto \gamma_{\rm m}^2 B$, with $\gamma_{\rm m} = \gamma_{dn}$ and $B \propto \sqrt{e_{\rm int}}$,

$$\nu_{\rm m} \propto C_u R^{-3/2}. \tag{K13}$$

For $\nu_{\rm G} > \nu_{\rm sa}$, the spectral luminosity is therefore

$$L_{\nu,{\rm G}} \propto L_{\nu,\max}\nu_{\rm m}^{(p-1)/2}\nu_{\rm G}^{(1-p)/2} \times \propto C_u^{(p+5)/2}R^{-[3(p+1)]/4}\nu_{\rm G}^{(1-p)/2}. \tag{K14}$$

Using $R = C_u^{2/(5-k)}R_0$ and $D_0 = 2R_0$, we obtain

$$L_{\nu,{\rm G}} \propto \left(C_u^{\rm ST}\right)^{\frac{(2-k)p+22-5k}{2(5-k)}} D_0^{-\frac{3(p+1)}{4}}. \tag{K15}$$

The corresponding surface brightness is

$$\Sigma_{\rm G} = \frac{L_{\nu,{\rm G}}}{\pi^2 D^2}, \tag{K16}$$

and hence

$$\Sigma_{\rm G} \propto C_u^{(p+5)/2}R^{-[(3p+11)]/4}. \tag{K17}$$

Substituting $R = C_u^{2/(5-k)}R_0$ gives

$$\Sigma_{\rm G} \propto \left(C_u^{\rm ST}\right)^{\frac{(2-k)p+14-5k}{2(5-k)}} D_0^{-\frac{(3p+11)}{4}}. \tag{K18}$$

Thus, the self-similar correction modifies only the normalization of the $L_{\nu,{\rm G}}$–D_0 and $\Sigma_{\rm G}$–D_0 relations, while retaining their power-law slopes. For $k = 0$ and $p = 2.3$, the self-similar correction factor C_u increases the surface brightness by a factor of $\sim$1.2 which is again an order-of-unity effect.

ORCID iDs

Sk. Minhajur Rahaman https://orcid.org/0000-0003-1214-0521
Jonathan Granot https://orcid.org/0000-0001-8530-8941
Paz Beniamini https://orcid.org/0000-0001-7833-1043

References

Acharya, S. K., Beniamini, P., & Hotokezaka, K. 2025, A&A, 693, A108
Balasubramanian, A., Corsi, A., Mooley, K. P., et al. 2022, ApJ, 938, 12
Barniol Duran, R., Whitehead, J. F., & Giannios, D. 2016, MNRAS, 462, L31
Bell, A. R. 1978, MNRAS, 182, 147
Beniamini, P., Gill, R., & Granot, J. 2022, MNRAS, 515, 555
Beniamini, P., & Lu, W. 2021, ApJ, 920, 109
Bietenholz, M. F., Bartel, N., Argo, M., et al. 2021, ApJ, 908, 75
Blandford, R., & Eichler, D. 1987, PhR, 154, 1
Blandford, R. D., & McKee, C. F. 1976, PhFl, 19, 1130
Blandford, R. D., & Ostriker, J. P. 1978, ApJL, 221, L29
Borkowski, J., Gotz, D., Mereghetti, S., et al. 2004, GCN, 1, 2920
Bykov, A., Romansky, V., & Osipov, S. 2022, Univ, 8, 32
Cameron, P. B., Chandra, P., Ray, A., et al. 2005, Natur, 434, 1112
Caprioli, D., & Spitkovsky, A. 2014, ApJ, 794, 46
Chevalier, R. A. 1982, ApJ, 258, 790
Chevalier, R. A., & Fransson, C. 1994, ApJ, 420, 268
Chevalier, R. A., & Fransson, C. 2006, ApJ, 651, 381
Chevalier, R. A., & Li, Z.-Y. 1999, ApJL, 520, L29
Cioffi, D. F., McKee, C. F., & Bertschinger, E. 1988, ApJ, 334, 252
De Colle, F., Ramirez-Ruiz, E., Granot, J., & Lopez-Camara, D. 2012, ApJ, 751, 57
Draine, B. T. 2011, Physics of the Interstellar and Intergalactic Medium (Princeton Univ. Press)
Duffell, P. C., & Laskar, T. 2018, ApJ, 865, 94
Eftekhari, T., Margalit, B., Omand, C. M. B., et al. 2021, ApJ, 912, 21
Gaensler, B. M., Kouveliotou, C., Gelfand, J. D., et al. 2005, Natur, 434, 1104
Gelfand, J. D., Lyubarsky, Y. E., Eichler, D., et al. 2005, ApJL, 634, L89
Granot, J. 2007, RMxAC, 27, 140
Granot, J., & Piran, T. 2012, MNRAS, 421, 570
Granot, J., & Ramirez-Ruiz, E. 2012, in Gamma-ray Bursts, ed. C. Kouveliotou, R. A. M. J. Wijers, & S. Woosley (Cambridge Univ. Press), 215
Granot, J., Ramirez-Ruiz, E., & Loeb, A. 2005, ApJ, 618, 413
Granot, J., & Sari, R. 2002, ApJ, 568, 820
Granot, J., Ramirez-Ruiz, E., Taylor, G. B., et al. 2006, ApJ, 638, 391
Green, D. A. 2025, JApA, 46, 14
Gupta, S., Caprioli, D., & Spitkovsky, A. 2024, ApJ, 976, 10
Huang, Y. F., & Cheng, K. S. 2003, MNRAS, 341, 263
Kamble, A., Soderberg, A. M., Chomiuk, L., et al. 2014, ApJ, 797, 2
Kathirgamaraju, A., Giannios, D., & Beniamini, P. 2019, MNRAS, 487, 3914
Kawaguchi, K., Fujibayashi, S., Hotokezaka, K., Shibata, M., & Wanajo, S. 2022, ApJ, 933, 22
Kyutoku, K., Ioka, K., & Shibata, M. 2014, MNRAS, 437, L6
Ligorini, A., Niemiec, J., Kobzar, O., et al. 2021a, MNRAS, 501, 4837
Ligorini, A., Niemiec, J., Kobzar, O., et al. 2021b, MNRAS, 502, 5065
Matsuoka, T., Maeda, K., & Chen, K.-J. 2025, ApJL, 988, L53
Metzger, B. D., & Piro, A. L. 2014, MNRAS, 439, 3916
Moriya, T. J. 2014, AstHe, 107, 107
Nakar, E., & Piran, T. 2011, Natur, 478, 82
Nayana, A. J., Margutti, R., Wiston, E., et al. 2025, ApJ, 985, 51
Ostriker, J. P., & McKee, C. F. 1988, RvMP, 60, 1
Panaitescu, A., & Kumar, P. 2000, ApJ, 543, 66
Panaitescu, A., & Mészáros, P. 1999, ApJ, 526, 707
Pavlovic, M. Z., Dobardzic, A., Vukotic, B., & Urosevic, D. 2014, SerAJ, 189, 25
Petruk, O. 2000, A&A, 357, 686
Piran, T., Nakar, E., & Rosswog, S. 2013, MNRAS, 430, 2121
Radice, D., Galeazzi, F., Lippuner, J., et al. 2016, MNRAS, 460, 3255
Rassel, M., Kilian, P., Aberham, V., et al. 2023, ApJ, 952, 165
Reynolds, S. P. 1998, ApJ, 493, 375
Reynolds, S. P., Williams, B. J., Borkowski, K. J., & Long, K. S. 2021, ApJ, 917, 55
Ricci, R., Troja, E., Bruni, G., et al. 2021, MNRAS, 500, 1708
Sadeh, G., Linder, N., & Waxman, E. 2024, MNRAS, 531, 3279

Sari, R., Piran, T., & Narayan, R. 1998, ApJL, 497, L17
Sedov, L. I. 1959, Similarity and Dimensional Methods in Mechanics (Academic Press)
Sekiguchi, Y., Kiuchi, K., Kyutoku, K., Shibata, M., & Taniguchi, K. 2016, PhRvD, 93, 124046
Shibata, M., & Hotokezaka, K. 2019, ARNPS, 69, 41
Sironi, L., & Giannios, D. 2013, ApJ, 778, 107
Soderberg, A. M., Kulkarni, S. R., Berger, E., et al. 2005, ApJ, 621, 908
Spitkovsky, A. 2008, ApJL, 682, L5
Sutherland, R. S., & Dopita, M. A. 1993, ApJS, 88, 253
Taylor, G. B., & Granot, J. 2006, MPLA, 21, 2171
Taylor, G. B., Gelfand, J. D., Gaensler, B. M., et al. 2005, ApJL, 634, L93
Taylor, G. I. 1950, RSPSA, 201, 159
van Haarlem, M. P., Wise, M. W., Gunst, A. W., et al. 2013, A&A, 556, A2
Wang, H., Beniamini, P., & Giannios, D. 2024, MNRAS, 527, 5166
Weltman, A., Bull, P., Camera, S., et al. 2020, PASA, 37, e002